JGR Atmospheres

RESEARCH ARTICLE
10.1029/2023JD039272

A Cold Lid on a Warm Ocean: Indian Ocean Surface Rain Layers and Their Feedbacks to the Atmosphere

Kyle Shackelford[1], Charlotte A. DeMott[1], Peter Jan van Leeuwen[1], Matthew R. Mazloff[2], and Rui Sun[2]

[1]Department of Atmospheric Science, Colorado State University, Fort Collins, CO, USA, [2]Scripps Institution of Oceanography, University of California, San Diego, CA, USA

Key Points:

- Cold and statically stable freshwater rain layers (RLs) warm the subsurface ocean by reducing nocturnal vertical mixing
- RL-induced surface cooling and sub-surface warming first delay, but then enhance the development of deep convection within the Madden-Julian Oscillation (MJO)
- RL regulation of convective intensity may thus play a role in setting MJO period and propagation speed

Correspondence to:
K. Shackelford,
Kyle.Shackelford@colostate.edu

Citation:
Shackelford, K., DeMott, C. A., Jan van Leeuwen, P., Mazloff, M. R., & Sun, R. (2024). A cold lid on a warm ocean: Indian Ocean surface rain layers and their feedbacks to the atmosphere. *Journal of Geophysical Research: Atmospheres*, *129*, e2023JD039272. https://doi.org/10.1029/2023JD039272

Received 18 MAY 2023
Accepted 10 JAN 2024

Author Contributions:
Conceptualization: Kyle Shackelford, Charlotte A. DeMott, Peter Jan van Leeuwen
Data curation: Kyle Shackelford
Formal analysis: Kyle Shackelford, Charlotte A. DeMott, Peter Jan van Leeuwen
Funding acquisition: Charlotte A. DeMott, Peter Jan van Leeuwen
Investigation: Kyle Shackelford
Methodology: Kyle Shackelford, Charlotte A. DeMott, Peter Jan van Leeuwen, Matthew R. Mazloff, Rui Sun
Project Administration: Charlotte A. DeMott, Peter Jan van Leeuwen
Resources: Charlotte A. DeMott, Matthew R. Mazloff, Rui Sun
Software: Kyle Shackelford, Matthew R. Mazloff, Rui Sun

Abstract Ocean surface rain layers (RLs) form when relatively colder, fresher, less dense rain water stably stratifies the upper ocean. RLs cool sea surface temperature (SST) by confining surface evaporative cooling to a thin near-surface layer, and generate sharp SST gradients between the cool RL and the surrounding ocean. In this study, ocean-atmosphere coupled simulations of the November 2011 Madden-Julian Oscillation (MJO) event are conducted with and without RLs to evaluate two pathways for RLs to influence the atmosphere. The first, termed the "SST gradient effect," arises from the hydrostatic adjustment of the boundary layer to RL-enhanced SST gradients. The second, termed the "SST effect," arises from RL-induced SST reductions impeding the development of deep atmospheric convection. RLs are found to sharpen SST gradients throughout the MJO suppressed and suppressed-to-enhanced convection transition phases, but their effect on convection is only detected during the MJO suppressed phase when RL-induced SST gradients enhance low-level convergence/divergence and broaden the atmospheric vertical velocity probability distribution below 5 km. The SST effect is more evident than the SST gradient effect during the MJO transition phase, as RLs reduce domain average SST by 0.03 K and narrow vertical velocity distribution, thus delaying onset of deep convection. A delayed SST effect is also identified, wherein frequent RLs during the MJO transition phase isolate accumulated subsurface ocean heat from the atmosphere. The arrival of strong winds at the onset of the MJO active phase erodes RLs and releases subsurface ocean heat to the atmosphere, supporting the development of deep convection.

Plain Language Summary Rain water is less dense than near-surface ocean water. For this reason, rain water can float on the ocean surface following rain events and form a "rain layer" in the upper ocean. Rain layers that form in the tropical Indian Ocean reduce sea surface temperature (SST) and shield the subsurface ocean below the rain layer from the atmosphere, thus altering heat exchange between the ocean and atmosphere. In this study, we conduct model experiments over the tropical Indian Ocean to investigate rain layer feedbacks to the atmosphere. We identify two potential rain layer feedback mechanisms, one in which rain-enhancement of SST gradients contributes to the formation of clouds and precipitation in the atmosphere, and a second in which rain-driven SST reduction suppresses the development of clouds and precipitation. Our results indicate that rain-driven SST reduction is the dominant immediate feedback, as clouds and precipitation are reduced in the presence of rain layers. A delayed rain layer feedback is also identified, wherein rain layers insulate subsurface ocean heat from the atmosphere. When rain layers are destroyed by wind-driven mixing, the stored ocean heat is released to the atmosphere, and supports the development of clouds and precipitation.

1. Introduction

The Madden-Julian Oscillation (MJO) is an eastward propagating, planetary scale convective disturbance that circumnavigates the global tropics on time scales of 30–60 days (Madden & Julian, 1971). MJO influence on tropical climate ranges from intraseasonal time scales, where it is the dominant mode of tropical variability, to interannual time scales, where it influences the onset and evolution of El Niño Southern Oscillation events (e.g., McPhaden et al., 1988). In addition to it's impact on tropical climate, diabatic heating anomalies from MJO convection perturb circulations in the extratropics and represent an important source of extratropical atmospheric predictability on subseasonal time scales (Hoskins & Karoly, 1981; Weickmann, 1983; Vitart, 2017; Tseng et al., 2019; Wang et al., 2020; Stan et al., 2022).

Supervision: Charlotte A. DeMott, Peter Jan van Leeuwen
Validation: Kyle Shackelford
Visualization: Kyle Shackelford
Writing – original draft: Kyle Shackelford, Charlotte A. DeMott, Peter Jan van Leeuwen
Writing – review & editing: Kyle Shackelford, Charlotte A. DeMott, Peter Jan van Leeuwen, Matthew R. Mazloff, Rui Sun

Over the Indian and western Pacific Oceans, the MJO manifests as coupled regions of enhanced and suppressed cloudiness, referred to as the MJO active and suppressed phases, respectively. From the Eulerian perspective of the central Indian Ocean, an MJO event starts with the suppressed phase, characterized by large-scale subsidence, calm winds, shallow convection, light rainfall, and high outgoing longwave radiation (OLR) (Johnson et al., 1999). As the disturbance propagates eastward, MJO suppressed conditions are gradually replaced with MJO active conditions, characterized by large-scale rising motion, increased winds, deep convection, heavy rainfall, and reduced OLR. Because of the slow propagation speed (~4–5 m s^{-1}) and large-scale nature of the MJO, the transition from convectively suppressed to convectively enhanced regimes occurs gradually over the course of several days. For this reason, it's helpful to define an intermediate MJO phase that describes the characteristics distinct to this transition period, referred to as the "transition" phase by the atmospheric science community (e.g., Ruppert & Johnson, 2016). The MJO transition phase is characterized by an increase in cumulus congestus clouds and increasing rainfall relative to the suppressed phase, but without the strong westerly winds and deep convection evident during the active phase (Johnson et al., 1999; Moum et al., 2014; Thompson et al., 2019).

During the MJO transition phase, the vertical structure of ocean mixing is distinctly different from that observed during either the MJO suppressed or active phases (Pujiana et al., 2018; Thompson et al., 2019). The oceanography community refers to this period as the "disturbed" phase. For reasons that will become evident later in study, we hereafter refer to the MJO transition phase as the disturbed phase, since the emphasis of this study is the ocean's influence on the MJO.

In the tropical warm pool, the ocean mixed layer temperature, salinity, and stability are strongly forced by surface meteorology (Anderson et al., 1996; Halkides et al., 2015; Lau & Sui, 1997; Weller & Anderson, 1996). During the MJO suppressed phase, the combination of light winds and enhanced surface solar heating warms the upper ocean and induces a stable temperature stratification, forming stable near-surface diurnal warm layers (DWLs; e.g. Bellenger & Duvel, 2009; Soloviev & Lukas, 1997; Woolnough et al., 2007). Overnight, net surface heat flux out of the ocean cools and destabilizes the upper ocean, deepening the ocean mixed layer (Bellenger & Duvel, 2009; Thompson et al., 2019; Woods & Barkmann, 1986; Woolnough et al., 2007).

Increased rainfall during the MJO disturbed phase deposits relatively colder, fresher, and less dense rain water on the ocean surface. Because wind speeds remain low to moderate during the disturbed phase, the less dense rain water frequently acts to stably stratify the upper ocean, forming near-surface rain layers (RLs; e.g. Asher et al., 2014; Drushka et al., 2016; Reverdin et al., 2012; Shackelford et al., 2022; Thompson et al., 2019; Wijesekera et al., 1999). Unlike DWLs, which are stabilized by a temperature gradient, RLs are stabilized by a salinity gradient and are more resistant to destruction via nocturnal convection (Thompson et al., 2019). While DWLs and RLs can occur during all MJO phases, and can be present simultaneously, DWLs are most frequent during the MJO suppressed phase and RLs are most frequent during the MJO disturbed phase (Shackelford et al., 2022; Thompson et al., 2019). During the MJO active phase, the stabilizing buoyancy flux from surface heat and freshwater inputs is typically insufficient to withstand mixing by strong surface winds (Moum et al., 2014; Shackelford et al., 2022; Thompson et al., 2019). Thus, the ocean frequently becomes well-mixed to the thermocline with a diurnally uniform SST during this period.

Ocean turbulent heat fluxes feed back to MJO convection through SST variability that is largely driven by MJO forcing and regulated by ocean stable layers. Anomalous high SST in DWLs during the suppressed phase enhances turbulent heat fluxes and reduces convective inhibition. This effect initiates convection and facilitates column moistening that "preconditions" the free troposphere to deep convection prior to the active MJO (Ruppert Jr. & Johnson, 2016). Additionally, increased SSTs ahead of MJO convection may support propagation and maintenance of MJO convection by enhancing surface fluxes and frictional moisture convergence (Wang & Rui, 1990a; de Szoeke et al., 2015; DeMott et al., 2016; Zhang & Anderson, 2003; Hudson & Maloney, 2022). SST gradient-induced moisture convergence may also play a role in recharging moist static energy prior to the active MJO (de Szoeke & Maloney, 2020).

The importance of ocean feedbacks to MJO convection is evidenced by improved representation of the MJO in coupled versus uncoupled model simulations (e.g., DeMott et al., 2015, 2019; Kemball-Cook et al., 2002; Woolnough et al., 2000, 2007; Zhang et al., 2006). In coupled simulations, high vertical resolution in the upper ocean and frequent ocean-atmosphere coupling further improve MJO representation, with the improvement in both cases attributed to better resolving the SST diurnal cycle (Bernie et al., 2005; Woolnough et al., 2007; Zhao & Nasuno, 2020).

While ocean feedback to the MJO via DWLs is well documented (Bellenger et al., 2010; de Szoeke et al., 2021; Ruppert Jr. & Johnson, 2016; Woolnough et al., 2000, 2007), the feedbacks associated with near-surface RLs to MJO convection are less explored. Regular observation of RLs has been limited by the coarse vertical resolution and infrequent sampling of buoys and Argo floats. Thus, most observations of RLs have been collected with ship-based measurements (Asher et al., 2014; Drushka et al., 2019; Iyer & Drushka, 2021; Thompson et al., 2019) and drifters equipped to profile the near-surface ocean (Reverdin et al., 2012), hindering observational analysis of RL feedbacks to the atmosphere.

Because of observational constraints, RL characteristics as a function of meteorological surface forcing and ocean background state are often described using idealized, single-column model experiments (Drushka et al., 2016; Iyer & Drushka, 2021). However, the idealized, 1D nature of these ocean simulations provide limited information on RL behavior under realistic surface forcing and on RL feedbacks to the atmosphere. Shackelford et al. (2022) studied RL formation under realistic atmospheric conditions by forcing a 2D array of 1D ocean column models using output from a convection-permitting simulation of the November 2011 DYNAMO event. Their findings are consistent with in situ observations of RLs analyzed by Thompson et al. (2019), and corroborate the results of previous model experiments (Pei et al., 2018) that RLs reduce local SST through the surface input of cold rain and sustain and enhance SST reductions through a stable salinity stratification that confines wind-driven evaporative cooling to the near-surface RL. Shackelford et al. (2022) also demonstrated the role of RLs in enhancing small-scale SST gradients that induce pressure perturbations in the atmospheric boundary layer and potentially excite atmospheric convection (Back & Bretherton, 2009; Li & Carbone, 2012; Lindzen & Nigam, 1987). Additionally, Pei et al. (2018) demonstrated that RLs may produce a slight subsurface ocean heating effect below the RL base. We hypothesize that this presents another potential mechanism for RLs to influence the atmosphere, in which statically stable RLs isolate the subsurface ocean from the atmosphere until wind mixing erodes RLs and exposes the atmosphere to previously shielded subsurface warm water. The incomplete understanding of RL feedbacks to the atmosphere motivates the following questions.

1. What is the relative importance of RL generated SST gradients and RL-induced SST reduction in RL feedbacks to the atmosphere?
2. How does the frequent separation of the subsurface ocean and the atmosphere by RLs during the MJO disturbed phase feed back to MJO convection?

This study utilizes a regional coupled ocean-atmosphere model to investigate the nature of RL feedbacks to the atmosphere. Section 2 provides details on the model and our simulations. Feedbacks to the atmosphere by SST gradients and reduced SST in RLs are analyzed in Section 3, with an overall focus on how these effects vary as a function of MJO phase. We discuss the significance of these results in Section 4 before presenting a concise summary and final conclusions in Section 5.

2. Methods

A description of the Scripps-KAUST Regionally Integrated Prediction System (SKRIPS) is provided in Section 2.1. SKRIPS simulations used to evaluate RL feedbacks to the atmosphere are outlined in Section 2.2.

2.1. SKRIPS Model

The Scripps-KAUST Regionally Integrated Prediction System (SKRIPS) is a regional ocean-atmosphere coupled model developed in a collaborative effort between Scripps Institute of Oceanography and the King Abdullah University of Science and Technology (Sun et al., 2019). SKRIPS is comprised of an atmospheric solver, the Weather Research and Forecasting model (WRF; Skamarock et al., 2019), an ocean solver, the MITgcm (Marshall et al., 1997), and a coupler, the Earth Systems Modeling Framework (ESMF) coupled driver (Hill et al., 2004). The ESMF component is a two-way coupler that receives near-surface atmospheric variables (10-m u- and v-wind components, 2-m temperature and specific humidity, turbulent and radiative heat fluxes) and ocean surface conditions (SST and ocean surface velocity) that are then used to update the MITgcm surface forcing and WRF lower boundary conditions, respectively (Sun et al., 2019). Surface turbulent heat fluxes are computed by WRF using the COARE bulk flux algorithm (Fairall et al., 1996, 2003) and then passed to MITgcm by the coupler. SKRIPS output has been previously validated against atmosphere and ocean observations and reanalysis products in 30-day simulations of extreme heat events in the Red Sea region (Sun et al., 2019), and in 14-day hindcasts of atmospheric river events over the Pacific Ocean (Sun et al., 2021).

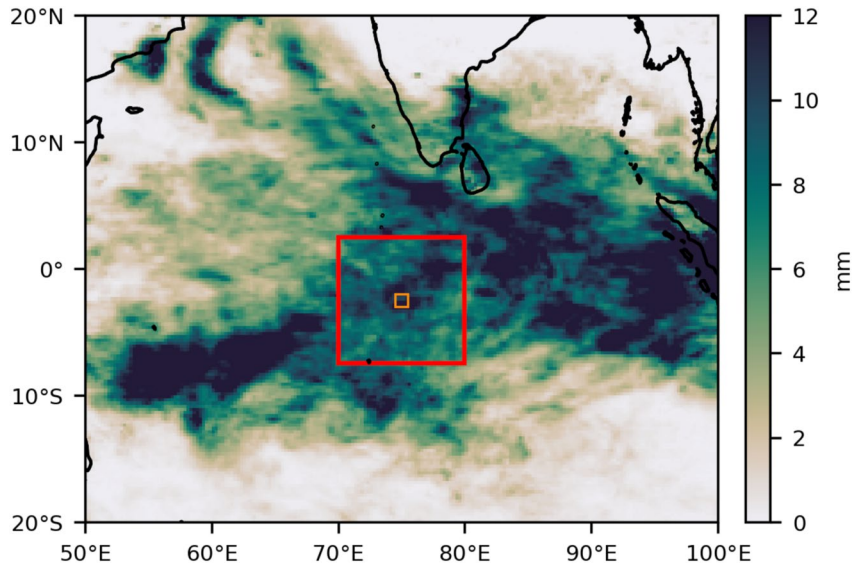

Figure 1. CMORPH daily average rainfall (mm) for November 2011. The 10° by 10° model domain is outlined in red and the inner model domain used for computing ocean stability profiles in Figure 4 is outlined in orange.

SKRIPS currently cannot account for the temperature of rain that falls onto the ocean surface, so rain temperature is effectively the same as that of the SST. In reality, the temperature of rain is more typically that of the near-surface wetbulb air temperature, which can be several °C cooler than the SST (Gosnell et al., 1995). The warm bias of rain temperature in SKRIPS could potentially over-stabilize the upper ocean and exaggerate the effects of RL feedbacks to the atmosphere. We compared near-surface temperature and salinity stratification in our SKRIPS simulation to that in a simulation of a 1D ocean mixing model with rain temperature set to the wetbulb temperature (Shackelford et al., 2022). The differences in temperature stratification between SKRIPS and the 1D model are small, and rain-driven changes to salinity stratification are much greater than rain-driven changes to temperature stratification in both SKRIPS and the 1D model. This is consistent with the findings of Thompson et al. (2019), which showed that positive buoyancy induced by rain freshening is an order of magnitude larger than negative buoyancy induced by rain cooling, and thus, warm rain temperature does not negatively influence the results of our study.

2.2. Model Experiments

We investigate RL feedbacks to the atmosphere by running a 29-day SKRIPS simulation over the tropical Indian Ocean from November 1–30, 2011. This time period and location coincides with the November 2011 MJO event that was observed and studied during the Dynamics of the Madden-Julian Oscillation field campaign (DYNAMO; Yoneyama et al., 2013) The model is configured for a 10° by 10° domain centered on 75°E and 2.5°S (Figure 1), with 2 km horizontal grid spacing in both the ocean and atmosphere. The 2 km horizontal grid spacing supports a convection-permitting WRF simulation. At convection-permitting scales (1–4 km), horizontal grid-spacing begins to approach the size of individual convective elements, "permitting" the removal of convective parameterizations from model simulations (Lucas-Picher et al., 2021). The fine-scale horizontal grid spacing of these simulations provides a detailed depiction of both atmospheric convection and the upper ocean temperature and salinity response to rainfall, both of which are critical in evaluating RL influence on the atmosphere.

Vertically, MITgcm is initialized on a stretched grid of 78 levels to a depth of 69.1 m, with 10 cm grid-spacing in the upper 2 m of the ocean and a telescoping vertical grid below 2 m. The MITgcm time step is 60 s and sub-grid scale horizontal mixing is parameterized using nonlinear Smagorinsky viscosities, while sub-grid scale vertical mixing is parameterized using the *K*-profile parameterization (Large et al., 1994). WRF is initialized with 35 vertical sigma levels and a model top of 50 hPa. A summary of WRF parameterizations can be found in Table 1. Initial and boundary conditions are provided by ERA-5 for the atmosphere (Hersbach et al., 2020) and Hybrid Coordinate Ocean Model (HYCOM; Chassignet et al., 2007) reanalyzes for the ocean, with lateral boundary

Table 1
Weather Research and Forecasting Parameterizations

Longwave radiation	Rapid radiative transfer model for GCMs (Iacono et al., 2008)
Shortwave radiation	Rapid Radiative Transfer Model for GCMs (Iacono et al., 2008)
Microphysics scheme	Morrison 2-moment (Morrison et al., 2005)
PBL scheme	Mellor–Yamada–Nakanishi–Niino (Nakanishi & Niino, 2009)
Surface layer	Revised MM5 scheme (Jiménez et al., 2012)
Radiation time step	2 min
Model time step	10 s

forcing applied to both every 3 hr. WRF-MITgcm coupling frequency is set to 60 s, at which point WRF lower boundary forcing and MITgcm surface forcing are updated and applied.

To investigate the impact of RLs on the atmosphere, we conduct a second simulation over this domain with an identical model setup except that precipitation flux passed from WRF to MITgcm by the ESMF coupler is set to 0.0 at every time step. Therefore, in this second simulation, precipitation generated by WRF is prevented from falling on the ocean surface. We refer to the control experiment as *RL* and this second simulation as *no-RL*.

3. RL Feedbacks to the Atmosphere

Here, we investigate two pathways in which RLs have the potential to influence the atmosphere. The first is the "SST gradient effect," wherein RL-induced SST gradients induce locally enhanced boundary layer convergence and divergence patterns that can regulate convective initiation (Li & Carbone, 2012, Section 3.1). The second, the more general "SST effect," describes both the direct effect of local SST reduction within RLs on atmospheric convection, and the delayed effect RL static stability may have on SST, and turbulent heat fluxes, by isolating the subsurface ocean from the atmosphere (Section 3.2).

3.1. The SST Gradient Effect

The SST gradient effect refers to the hydrostatic adjustment of the marine boundary layer to SST gradients that force pressure-induced wind accelerations and drive patterns of low-level convergence and divergence (Back & Bretherton, 2009; Li & Carbone, 2012; Lindzen & Nigam, 1987). While SST gradients that exist on large spatial scales (≥100 km) and long time scales (≥1 day) are accepted as a frequent precursor to atmospheric convection, the transient nature and smaller-scale of rain-induced SST gradients have presented challenges in evaluating their impact on the atmosphere. We expect RLs to sharpen SST gradients in the *RL* simulation compared to the *no-RL* simulation during the MJO suppressed and disturbed phases. In the atmosphere, locally enhanced boundary layer convergence from RL-induced SST gradients could lead to convective initiation, in a manner similar to that shown by Li and Carbone (2012) for SST gradients on 25 km scales. An increase in the frequency of strong vertical updrafts in the *RL* simulation during MJO suppressed and disturbed phases would be indicative of the RL-SST gradient-convergence-convection feedback.

Li and Carbone (2012) showed theoretically that, for the West Pacific warm pool, the time derivative of surface wind divergence is proportional to the Laplacian of the SST field ($\nabla^2 SST$). Hence, we compute $\nabla^2 SST$ for both *RL* and *no-RL* at each grid cell to evaluate the role of RLs in generating and enhancing spatial SST gradients. $\nabla^2 SST$ is computed with adjacent grid cells using a 5-point stencil, and $\nabla^2 SST$ distribution for the two simulations composited by MJO phase can be seen in Figure 2. To quantify differences in the two distributions, we take the median of the absolute value of $\nabla^2 SST$ as an approximation of the width parameter of the underlying distribution, which reveals roughly a factor of two increase in the $\nabla^2 SST$ width parameter for *RL* (0.029) compared to *no-RL* (0.014) over the entire simulation. The factor of two increase in $\nabla^2 SST$ width parameter is consistent with findings of similarly constrained experiments conducted in an ocean environment with 1-dimensional dynamics (Shackelford et al., 2022). RL enhancement of SST gradients is most pronounced during the disturbed MJO, when $\nabla^2 SST$ width parameter is nearly tripled in *RL* (0.048) compared to *no-RL* (0.017), while SST gradients in both simulations were greatly reduced during the active phase with *RL* and *no-RL* $\nabla^2 SST$ width parameters less

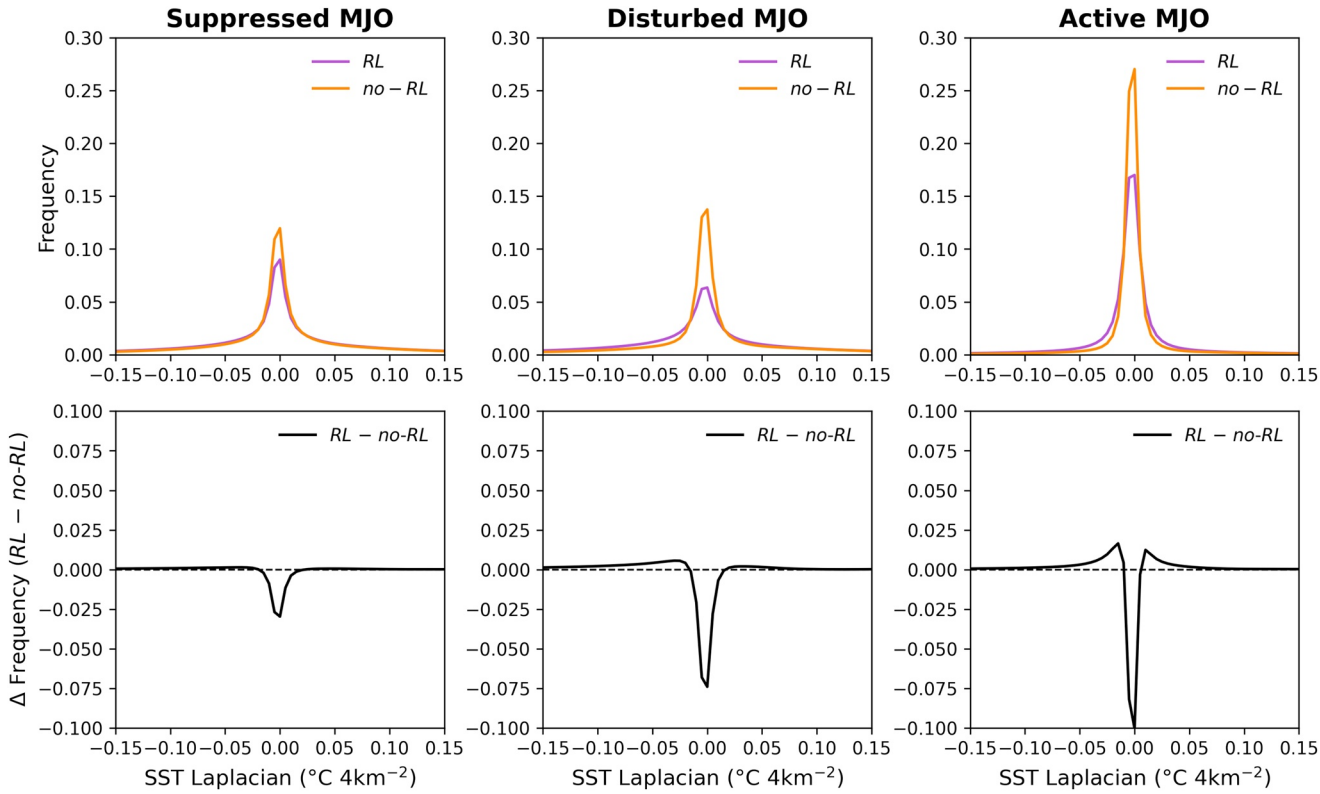

Figure 2. Top: distribution of sea surface temperature (SST) Laplacian for rain layer (*RL*) (purple) and *no-RL* (orange), composited column-wise by Madden-Julian Oscillation (MJO) phase. Bottom: change in SST Laplacian frequency (*RL*−*no-RL*), composited column-wise by MJO phase. Note that while difference in the MJO active phase *RL* and *no-RL* distributions appear quite large, both distributions are narrowly peaked around 0 and large SST gradients in both simulations are uncommon during MJO active phase.

than 0.01 (Figure 2). Comparisons of *RL* and *no-RL* $\nabla^2 SST$ distributions in the form of a Kolmogorov-Smirnov test indicates that differences between the two distributions are significant at a 95% confidence threshold across all three MJO phases (not shown).

RL feedback to the atmosphere through the SST gradient effect is evaluated by viewing the temporal coincidence between enhanced SST gradients and enhanced low-level convergence and divergence. Figure 3 displays time series of (from top to bottom): $\nabla^2 SST$ spatial variance for *RL* and *no-RL*, 10 m divergence spatial variance for *RL* and *no-RL*, and percent change in 10 m divergence variance. Time series of $\nabla^2 SST$ variance for *RL* and *no-RL* corroborate the findings of Figure 2 that RLs broaden the distribution of $\nabla^2 SST$ during the MJO suppressed and disturbed phases. The suppressed phase also features a 4 day period (11/05–11/09) in which 10 m divergence variance is roughly 5%–10% larger in *RL* than *no-RL* (Figure 3), and total accumulated rainfall is 6.2% higher in *RL* than *no-RL* (not shown). We revisit the coincident increase in rainfall and low-level divergence variance in the discussion section. This period coincides with increased $\nabla^2 SST$ variance in *RL*, consistent with our understanding that SST gradients can enhance boundary layer convergence and excite atmospheric convection.

Figure 2 demonstrates that SST gradients are largest in *RL* during the disturbed phase, and differences in $\nabla^2 SST$ variance between *RL* and *no-RL* are also most evident during the disturbed phase (Figure 3). However, 10 m divergence variance is reduced in *RL* relative to *no-RL* during the disturbed phase, suggesting that RL-induced SST gradients may only influence the atmosphere during the suppressed phase. We attribute the contrasting feedback of SST gradients between the suppressed and disturbed phases to changes in free tropospheric forcing between these two periods. In the suppressed phase, free troposphere forcing on the atmospheric boundary layer (e.g., latent heating above the trade wind inversion, downward momentum mixing, entrainment) is weak, thus, the influence of SST gradients on surface wind convergence/divergence is detectable. In the disturbed phase, free troposphere forcing on the atmospheric boundary layer is enhanced and free troposphere contributions to surface convergence/divergence overwhelm boundary layer contributions to surface convergence/divergence.

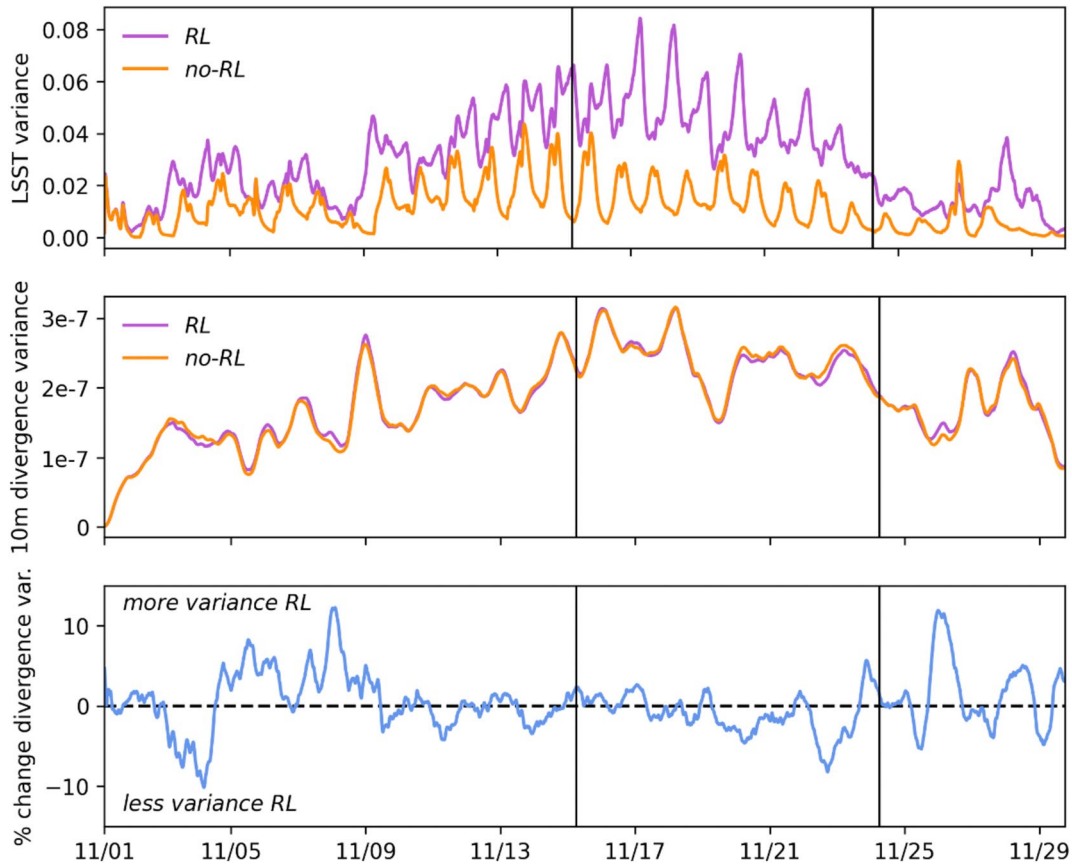

Figure 3. Time series of (from top to bottom): sea surface temperature Laplacian spatial variance for rain layers (*RL*) and *no-RL*, 10 m divergence spatial variance for *RL* and *no-RL*, and percent change in 10 m divergence (*RL*−*no-RL*). Divergence time series are presented as a 12-hr running mean. Vertical lines separate Madden-Julian Oscillation phase (suppressed phase: 11/01–11/15; disturbed phase: 11/15–11/24; active phase: 11/24–11/30).

SST gradients in the active phase are small in both simulations, and therefore not expected to feed back to the atmosphere (Figure 2). The influence of RL-driven SST gradients on horizontal organization of convection was evaluated using the organizational index (I_{org}), but results from this analysis were inconclusive (not shown).

3.2. The SST Effect

The SST effect refers to two distinct mechanisms in which RLs have the potential to influence the atmosphere by modifying SST. The *direct* SST effect results from RLs reducing SST locally through a stable salinity stratification that shoals ocean mixed-layer depth and confines evaporative cooling to a thin, near-surface layer. We expect the direct SST effect to be most pronounced during the MJO disturbed phase when RLs are frequently present and may hinder the development of atmospheric convection by reducing SST. The *delayed* SST effect arises from statically stable RLs isolating the subsurface ocean from the atmosphere. This separation of the subsurface ocean and atmosphere confines air-sea interaction to a near-surface cool layer, and limits exchange between the atmosphere and subsurface ocean heat in the presence of RLs. We expect the delayed SST effect to amplify MJO convection when surface winds are sufficiently strong to erode the RL and expose warm subsurface water to the atmosphere.

3.2.1. RL Influence on SST and the Surface Energy Budget

To evaluate the SST effect, it is useful to begin by viewing upper ocean stability in the *RL* simulation as a function of MJO state. Figure 4 shows a time series of mean values of rain rate, wind speed, downwelling shortwave radiation, the temperature component of the buoyancy frequency (N_T^2), the salinity component of the buoyancy frequency (N_S^2), and the total buoyancy frequency (N_{T+S}^2) for the *RL* simulation over a 1° by 1° subdomain centered

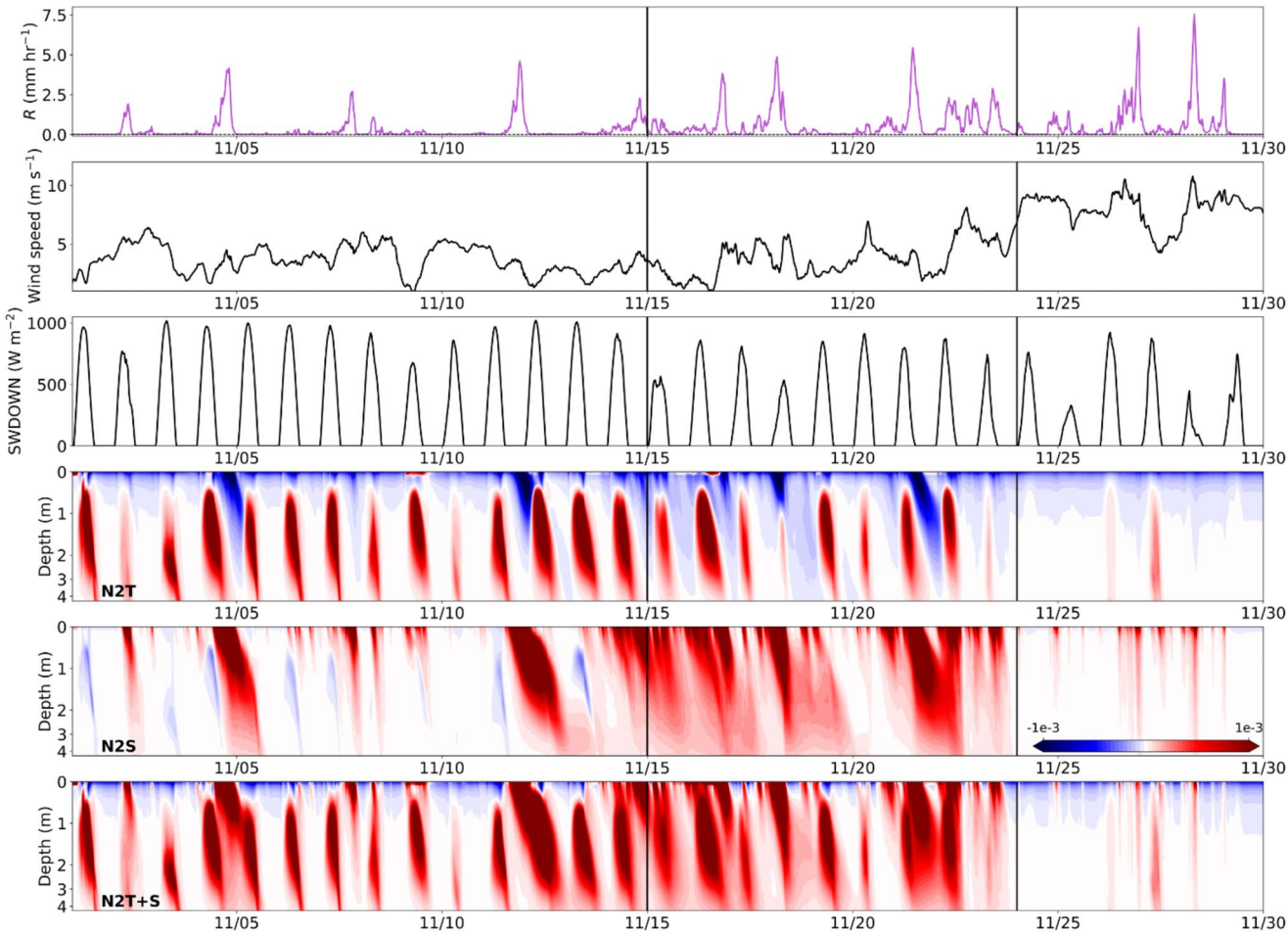

Figure 4. Time series of mean values for rain layer simulation over 1° by 1° subdomain of: rain rate (mm hr^{-1}), wind speed (m s^{-1}), downwelling shortwave radiation at ocean surface (W m^{-2}), the temperature component of the buoyancy frequency for the upper ∼4 m of the ocean (s^{-1}), the salinity component of the buoyancy frequency for the upper ∼4 m of the ocean (s^{-1}), total buoyancy frequency for the upper ∼4 m of the ocean (s^{-1}). 1° by 1° subdomain is centered within larger overall domain. Vertical lines separate Madden-Julian Oscillation phase. The N^2 color scale is consistent across N_T^2, N_S^2, N_{T+S}^2 (see colorbar in N_S^2 time series).

within the larger model domain (see Figure 1). Vertical lines separate MJO phase (suppressed: 11/01–11/15; disturbed: 11/15–11/24; active: 11/24–11/30). Viewing these time series over a smaller subdomain presents a more coherent signal of ocean response to surface forcing, as signals from individual precipitation events would be lost over a larger area. The three MJO phases exhibit distinct atmosphere and ocean characteristics, which are outlined below.

The MJO suppressed phase is characterized by infrequent rainfall, low winds, and high amounts of solar radiation impinging upon the ocean surface (Figure 4). Upper ocean stability is dominated by a diurnal cycle in N_T^2 and N_{T+S}^2, driven by daytime stabilization through DWLs and nocturnal convection mixing upper ocean heat downward and deepening the ocean mixed layer. Sparse precipitation during the suppressed phase results in a generally well-mixed upper ocean with respect to N_S^2, but low wind speeds enable the upper ocean to become readily stabilized during occasional periods of enhanced rainfall (e.g., 11/04, 11/13).

The MJO disturbed phase features increasing rainfall, decreasing downwelling solar radiation, and gradually increasing wind speeds (Figure 4). This corresponds to an upper ocean that is frequently stably stratified near the surface with respect to N_S^2 and N_{T+S}^2, reflecting the nearly constant presence of RLs during the disturbed phase. Note that for RLs in both the MJO suppressed and disturbed phases, salinity stabilization (N_S^2) far exceeds temperature destabilization (N_T^2), which allows the instability in the temperature stratification to persist within the overall statically stable column. While DWLs are present during the disturbed phase, their amplitude and frequency are reduced.

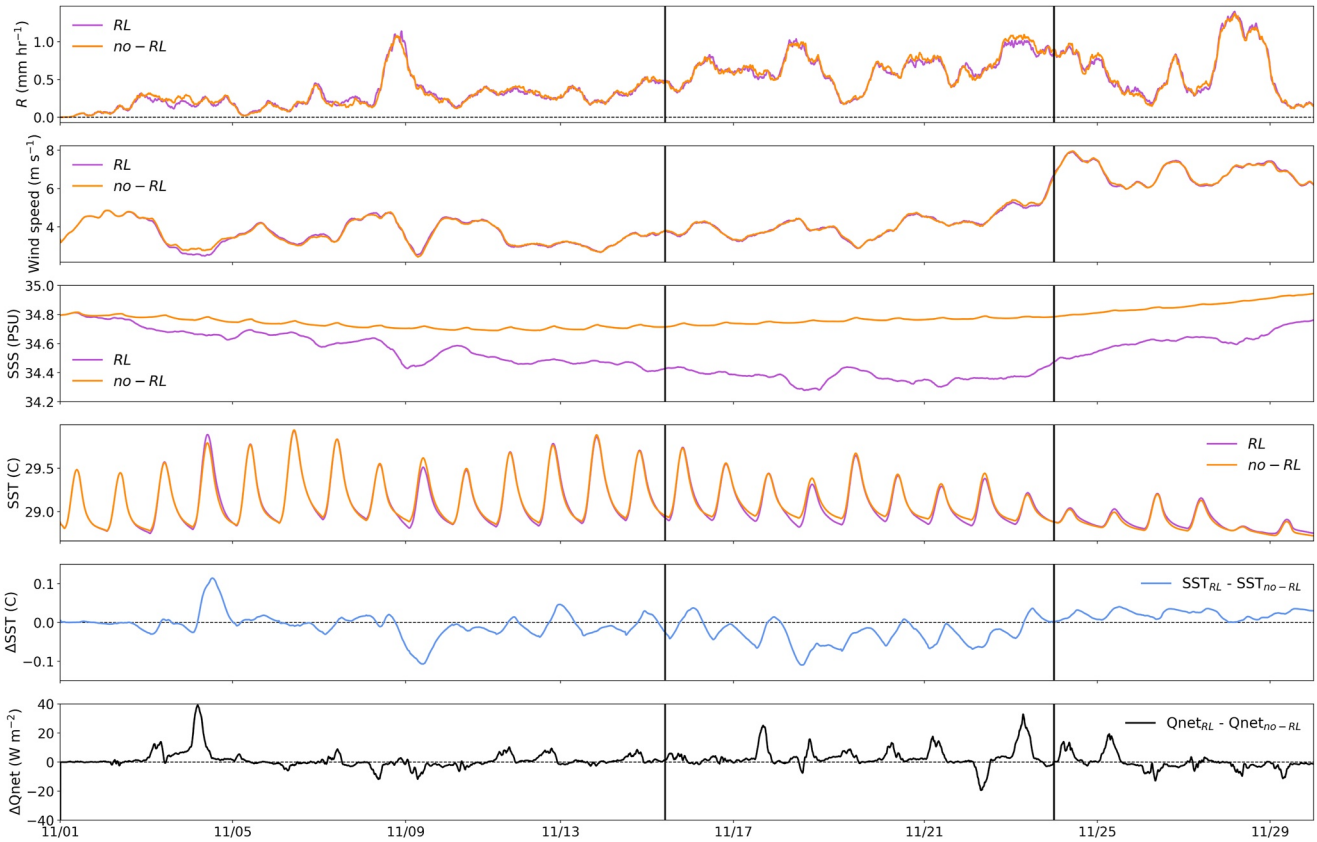

Figure 5. Time series of domain mean values for rain layer (*RL*) (purple) and *no-RL* (orange) from top to bottom: rain rate (mm hr^{-1}), wind speed (m s^{-1}), sea surface salinity (PSU, g kg^{-1}), sea surface temperature (SST) (C), SST difference ($SST_{RL} - SST_{no-RL}$), and net surface heat flux difference ($Q_{net;RL} - Q_{net;no-RL}$). Vertical lines separate Madden-Julian Oscillation phase (suppressed phase: 11/01–11/15; disturbed phase: 11/15–11/24; active phase: 11/24–11/30).

The MJO active phase is signified by a rapid increase in wind speeds followed by two large pulses of rainfall on November 26 and 28 (Figure 4). The convective envelope of the November 2011 MJO event consisted of two convectively coupled Kelvin waves, resulting in the double pulses in wind speed and rain rate in Figure 4 during the MJO active phase (Moum et al., 2014, 2016). While a brief relaxation in wind speed between the two pulses on November 27th allowed for transient, weak stabilization in both N_T^2 and N_S^2, wind bursts at the leading edge of the two Kelvin waves induced turbulent mixing in the upper ocean that inhibited the formation of near-surface stable layers.

To quantify the effect of RLs on SST and their feedback to the atmosphere over the MJO lifecycle, we return to comparisons between *RL* and *no-RL* simulations. Figure 5 displays time series of domain mean values for rain rate, wind speed, sea surface salinity (SSS), SST, SST difference (SST_{RL}–SST_{no-RL}), and net surface heat flux difference ($Q_{net;RL} - Q_{net;no-RL}$). Note that $Q_{net} > 0$ represents heat flux into the ocean, while $Q_{net} < 0$ represents heat flux into the atmosphere. While wind speed and moisture flux convergence (and hence rainfall) are constrained by boundary forcing and therefore appear similar in the two simulations, differences in SSS, SST, and Q_{net} are more evident. Since differences in SSS between the two simulations are expected, we focus on differences in domain mean SST and Q_{net} between *RL* and *no-RL*.

The SST difference time series reveals two clear signals as a function of MJO phase. First, lower domain average SST in *RL* relative to *no-RL* during the MJO disturbed phase (−0.029 K), and second, higher domain average SST in *RL* relative to *no-RL* during the MJO active phase (+0.022 K). Reduced SSTs with RLs develop during the disturbed phase despite +3.29 W m^{-2} more domain averaged ocean heating in *RL* than in *no-RL* (Figure 5). The disturbed phase SST reduction in *RL* is the result of frequent RL presence concentrating evaporative cooling in thin, near surface RLs (Shackelford et al., 2022). The physical explanation for higher SSTs in *RL* during the MJO active phase, however, is not consistent with surface forcing, as the mean net surface heat flux is reduced in

Table 2
Mean Value in Rain Layer (RL) Simulation ($\overline{x}$), Absolute Change Between RL and no-RL Simulation (Δ; RL−no-RL), and Percent Change Between RL and no-RL (%Δ; $\frac{\text{RL}-\text{no-RL}}{\text{RL}}$) as a Function of Madden-Julian Oscillation Phase for (Top to Bottom): Rain Rate (R), Sea Surface Temperature, Net Surface Heat Flux (Q_{net}), Net Surface Shortwave Heat Flux (SW_{net}), Net Surface Longwave Heat Flux (LW_{net}), Latent Heat Flux, Sensible Heat Flux, and Fraction of Domain Occupied by Cold Cloud Tops (CCF; OLR <115 W m^{-2})

Variable	Suppressed			Disturbed			Active		
	$\overline{x}$	Δ	%Δ	$\overline{x}$	Δ	%Δ	$\overline{x}$	Δ	%Δ
R (*mm hr*$^{-1}$)	0.25	−0.002	−0.86	0.61	−0.012	−2.01	0.59	0.005	0.83
SST (°*C*)	29.2	−0.005	−0.02	29.1	−0.029	−0.10	28.9	0.022	0.08
Q_{net} (*W m*$^{-2}$)	64.8	1.25	1.93	15.2	3.29	21.7	−64.6	−0.45	−0.69
SW_{net} (*W m*$^{-2}$)	256.0	0.82	0.32	204.7	1.93	0.94	163.3	0.22	0.13
LW_{net} (*W m*$^{-2}$)	−55.9	0.09	0.15	−49.1	0.02	0.05	−43.2	0.03	0.06
LHF (*W m*$^{-2}$)	−127.1	0.22	0.28	−129.2	1.20	0.93	−173.5	−0.61	−0.35
SHF (*W m*$^{-2}$)	−8.2	0.02	0.20	−11.2	0.14	1.27	−10.5	−0.08	−0.78
OLR (*W m*$^{-2}$)	247.64	0.92	0.37	195.29	0.64	0.33	169.64	−0.42	−0.25
CCF (*f*)	0.02	−0.0004	−2.05	0.15	−0.004	−3.38	0.23	0.007	3.05

RL compared to *no-RL* (−0.45 W m^{-2}). SST difference between *RL* and *no-RL* during the MJO disturbed phase is on the same order of magnitude as the standard error of domain mean SST, but standard error is larger than SST difference for all three MJO phases (not shown). We suspect this is more reflective of the relatively small effective sample size provided by a single MJO event, rather than the significance of SST differences between *RL* and *no-RL*. Additionally, SST differences of ∼0.03 K represent approximately 10%–15% of the SST range throughout composite MJO events (0.2–0.3 K; DeMott et al., 2016), indicating that RL-induced SST changes modulate MJO SST range by 10%–15%.

To better understand how RLs affect the net surface energy budget, we further investigate how each component of Q_{net} changes between *RL* and *no-RL* simulations for each MJO phase. Table 2 displays the *RL* simulation mean value ($\overline{x}$), *RL* minus *no-RL* absolute change (Δ), and *RL* minus *no-RL* percent change (%Δ) of rain rate, SST, Q_{net}, net surface shortwave heat flux (SW_{net}), net surface longwave heat flux(LW_{net}), latent heat flux (*LHF*), sensible heat flux (*SHF*), and cold cloud fraction (*CCF*; defined as the fractional area where *OLR* < 115 W m^{-2}) as a function of MJO phase. During the MJO suppressed and disturbed phases, differences in SW_{net}, LW_{net}, *LHF*, and *SHF* between *RL* and *no-RL* are all positive, indicating that all Q_{net} components enhance ocean heating and/or reduce ocean cooling in *RL*. However, SW_{net} changes are the dominant effect, accounting for 66% and 59% of total Q_{net} changes during the suppressed and disturbed phases, respectively. RL shoaling of the ocean mixed-layer depth allows approximately 50% (1 W m^{-2}) of the additional SW_{net} in *RL* to penetrate below the mixed-layer (Paulson & Simpson, 1977) and heat the subsurface ocean. We attribute the increase in SW_{net} with RLs to the 2.05% and 3.38% reductions in CCF during suppressed and disturbed conditions that allow more downward solar radiation to reach the surface in *RL* than in *no-RL*. *RL* minus *no-RL* changes to all Q_{net} component terms are roughly 1 W m^{-2} (1%) or less (Δ and %Δ columns in Table 1) during suppressed and disturbed conditions. Changes to Q_{net} itself, however, are larger, with an additional 1.25 W m^{-2} (+1.93%) ocean surface warming during suppressed conditions, and an additional 3.29 W m^{-2} (+21.7%) ocean surface warming during disturbed conditions. The implications of these RL-induced changes to Q_{net} are discussed further in Section 4.

Changes to *CCF* and Q_{net} with RLs during active conditions are opposite to those observed during the suppressed and disturbed conditions. In the active phase, *CCF* increases 3.05% and Q_{net} decreases by 0.45 W m^2 (0.69%). In contrast to suppressed and disturbed conditions, however, the decrease in Q_{net} is dominated by the combined changes in *LHF* and *SHF*, indicating greater ocean cooling in *RL* than in *no-RL*. Interestingly, active phase SW_{net} is larger in *RL* than in *no-RL*, despite the greater *CCF* in *RL*. We speculate that this could be the result of changes to convective organization with RLs, but more work is needed to understand this aspect of RL feedbacks to the atmosphere.

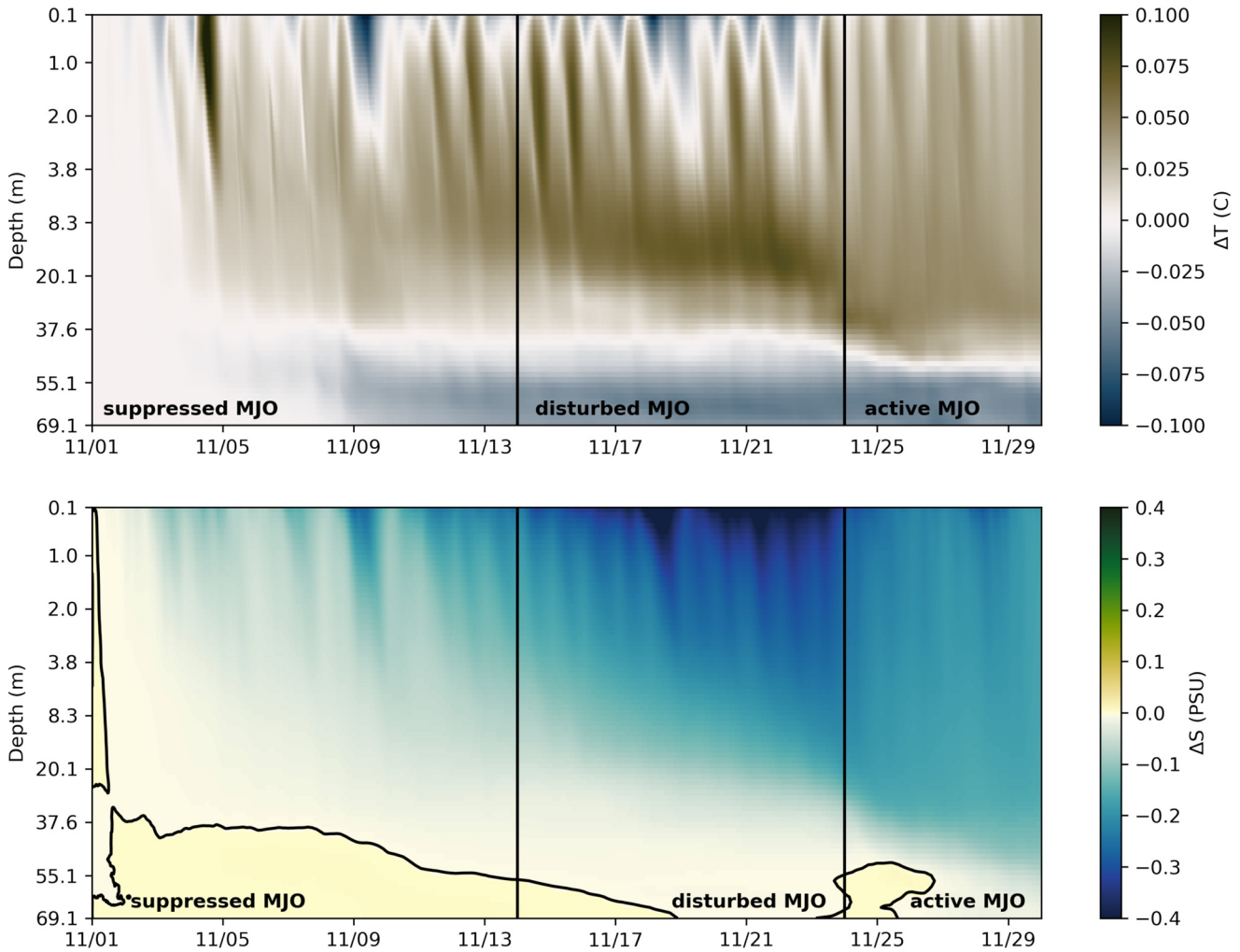

Figure 6. Top: Time series of domain mean vertical ocean temperature profile difference between rain layer (*RL*) and *no-RL* ($T_{RL} - T_{no-RL}$). Bottom: Time series of domain mean vertical ocean salinity profile difference between *RL* and *no-RL* ($S_{RL} - S_{no-RL}$). Vertical lines separate Madden-Julian Oscillation phase, and the black contour in the lower panel represents the zero-difference line.

3.2.2. RL Influence on Ocean Heat Content

Here, we present additional evidence that RL effects extend beyond the ocean surface. Particularly, they also regulate ocean heat content and the development of convection throughout the MJO lifecycle.

Figure 6 displays a vertical profile of domain mean ocean temperature and salinity difference between *RL* and *no-RL*. RL signatures can first be identified as instances of lower near-surface ocean temperature and salinity in *RL* during the MJO suppressed phase. During the MJO disturbed phase, these signatures increase in magnitude and frequency, reflecting the increasing presence of RLs as the MJO transitions from a convectively suppressed to convectively active state. Since RLs inhibit vertical mixing of surface waters with those of the deeper ocean (Reverdin et al., 2012; Shackelford et al., 2022; Thompson et al., 2019), cooling by surface evaporation in *RL* remains trapped near the ocean surface. Meanwhile, the reduced vertical mixing below the RL combined with the additional ∼1 W m^{-2} shortwave radiation that penetrates below the RL base amplify subsurface warming to a depth of about 40 m relative to the *no-RL* simulation. Offline calculations (not shown) indicate that enhanced SW_{net} penetrating below the RL base in *RL* accounts for 43% of the enhanced ocean heating between 2 and 40 m, while reduced vertical mixing below the RL base accounts for the other 57%. Below 40 m, the ocean is relatively cooler in *RL* with little salinity change, as the reduction of vertical mixing by RLs limits the vertical extent of downward mixing of heat and freshwater. The subsurface ocean near 40 m is thus stabilized, which reduces the entrainment of colder ocean water below 40 m in *RL* and

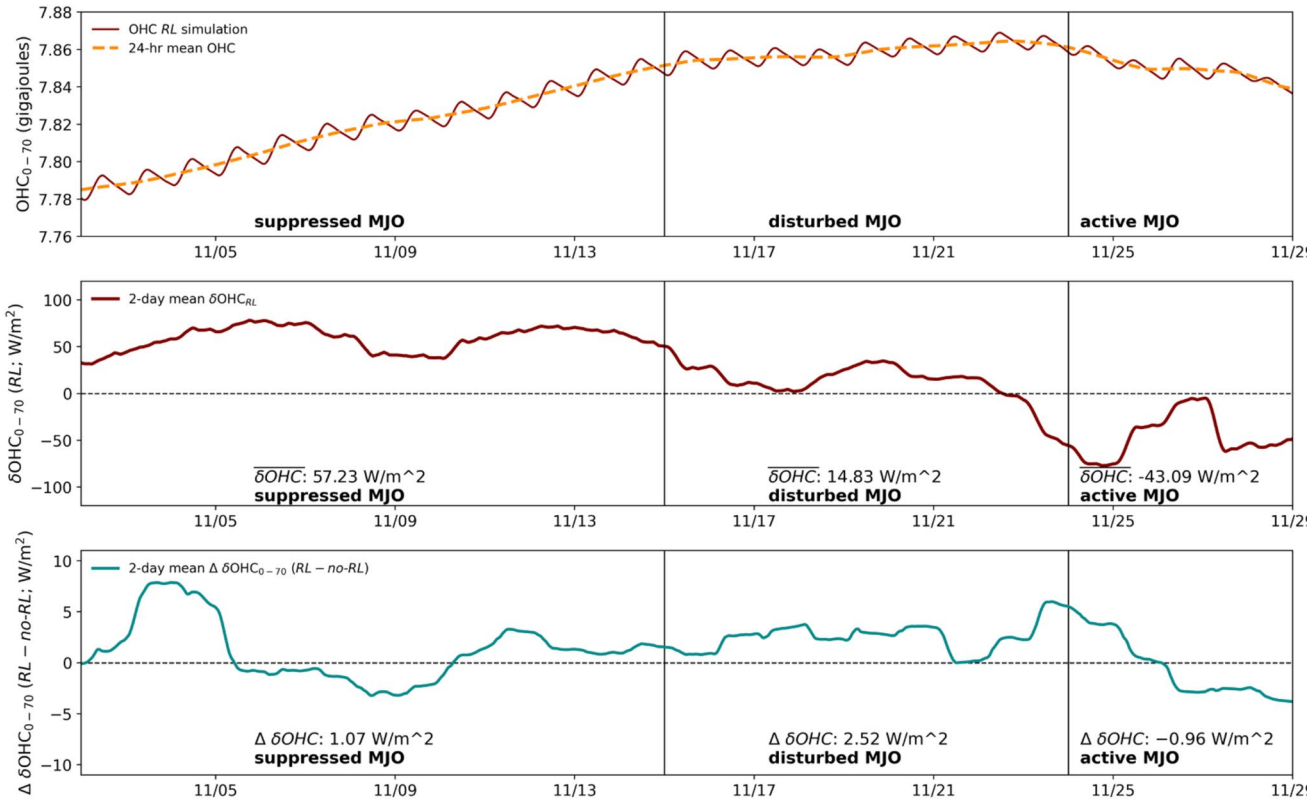

Figure 7. Top: time series of ocean heat content (OHC) and 24-hr running mean OHC for the entire ocean column (0–70 m) for the rain layer (*RL*) simulation. Middle: time series of 2-day running mean OHC change for each time step for the *RL* simulation (δOHC), displayed in units of W m^{-2}. Bottom: time series of 2-day running mean δOHC difference between *RL* and *no-RL* ($\Delta\delta$OHC). The values in the bottom two panels represent mean values in δOHC and $\Delta\delta$OHC for each Madden-Julian Oscillation phase.

further helps confine heat to the 2–40 m layer. This sequence represents a classic example of barrier layer formation by surface freshening (Cronin & McPhaden, 2002; McPhaden et al., 1988; Sprintall & Tomczak, 1992; You, 1998).

With the arrival of the MJO active phase, RLs are eroded and subsurface ocean heat previously trapped beneath the surface during the disturbed phase is mixed to the ocean surface, raising SST in *RL* relative to *no-RL*. Thus, the accumulation of subsurface heat in *RL* during the disturbed phase, and it's later release to the ocean surface during the active phase, presents a delayed pathway for the SST effect to feed back to MJO convection.

We quantify changes in subsurface ocean heat content (OHC) between *RL* and *no-RL* by computing OHC from 0 to 70 m for both simulations. Figure 7 shows a time series of OHC from 0 to 70 m for *RL* (top), OHC change at each time step for *RL* (δOHC; middle), and difference in OHC change between *RL* and *no-RL* ($\Delta\delta$OHC; bottom). The evolution of OHC in the *RL* simulation (Figure 7, top) shows that the gain, maintenance, and loss of OHC is distinct across the three MJO phases. OHC increases monotonically during the suppressed phase, increases at a slower rate during the disturbed phase, then decreases during the active phase with the onset of strong winds. The difference in OHC change between *RL* and *no-RL* ($\Delta\delta$OHC) also reveals a systematic regulation of ocean heat uptake by RLs across the three MJO phases. For the later half of the suppressed phase and the duration of the disturbed phase (11/10–11/24), $\Delta\delta$OHC is positive. This indicates that RLs allow the ocean to store more heat in *RL* than *no-RL* during this period by isolating the subsurface ocean from the effects of surface cooling. As the MJO transitions to the active phase, $\Delta\delta$OHC begins to decrease and become negative as a portion of the excess stored ocean heat in *RL* during the suppressed and disturbed phases is lost to the atmosphere through enhanced surface fluxes (Table 2). The large increase in $\Delta\delta$OHC on 11/03–11/04 (Figure 7) is associated with a short-lived, isolated convective disturbance in the northern region of the domain and is not associated with the large-scale envelope of MJO convection.

The physical mechanism for increased subsurface OHC in *RL* relative to *no-RL* becomes evident upon inspection of domain mean ocean stability profiles. Figure 8 shows time series of domain mean N_S^2, N_T^2 and N_{T+S}^2 for the two simulations, with solid black lines marking the top of the uppermost ocean stable layer and dashed lines marking

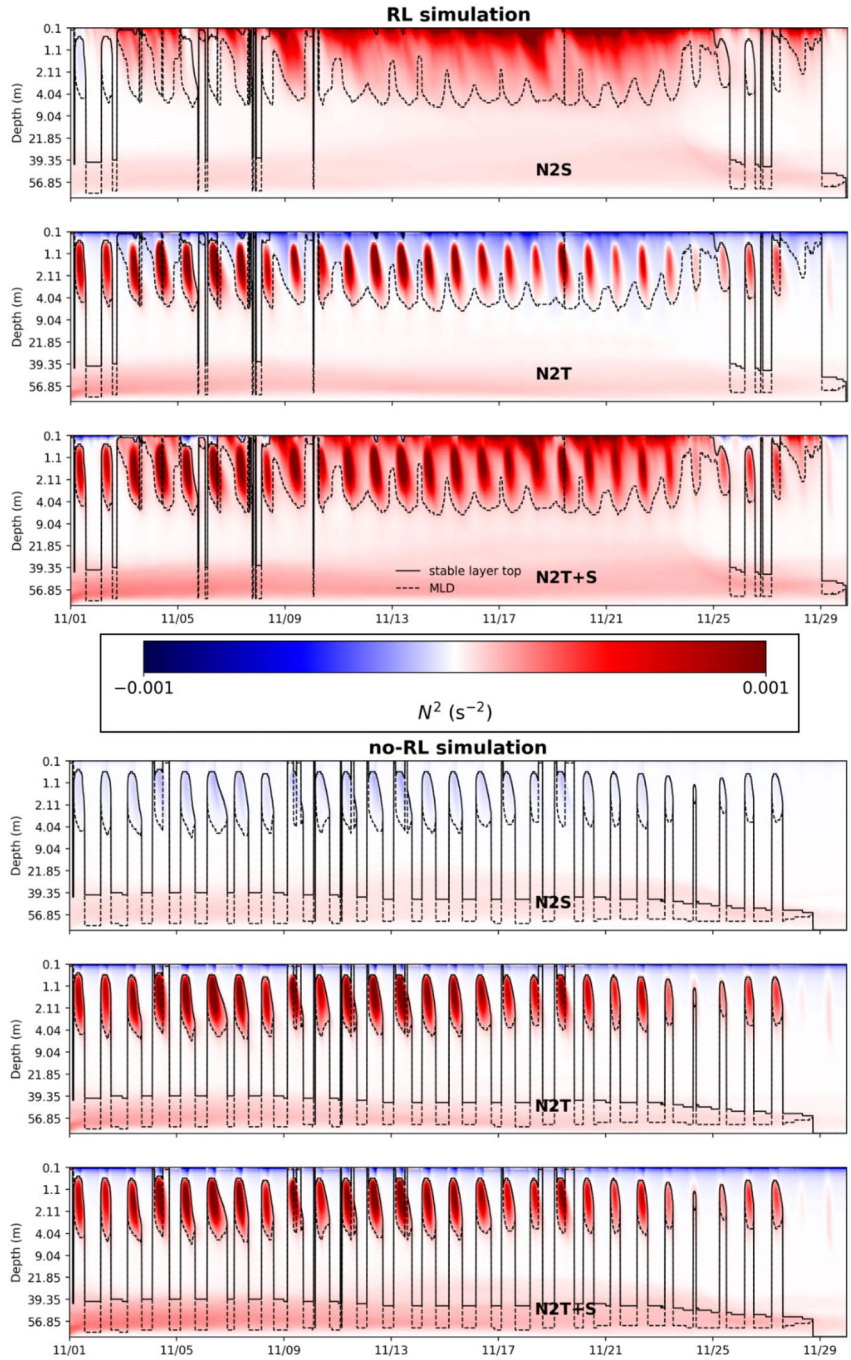

Figure 8. Time series of domain mean N_S^2, N_T^2, and N_{T+S}^2 for rain layer (*RL*) (top), and for *no-RL* (bottom). The solid lines marks the top of the uppermost stable layer, while the dashed line marks the bottom of the uppermost stable layer (e.g., mixed-layer depth). Note the depth intervals on the *y*-axis are displayed as a telescoping vertical grid.

the bottom of the uppermost stable layer (e.g., mixed-layer depth). We define an ocean layer as "stable" when $N_{T+S}^2 > 0.0001$. During the MJO suppressed phase, upper ocean stability exhibits a strong diurnal cycle in both *RL* and *no-RL*, as DWLs shoal the ocean mixed-layer during the day and nocturnal convection deepens the ocean mixed-layer overnight. However, occasional RLs during the suppressed phase reduce the frequency and duration of nocturnal convection in *RL*, which allows for subsurface OHC to accumulate in *RL* relative to *no-RL*. As the MJO transitions from suppressed to disturbed conditions, this effect becomes more apparent, when more frequent RLs stabilize the upper ocean and confine the ocean mixed-layer depth to <~4 m in *RL*. Because RLs are so

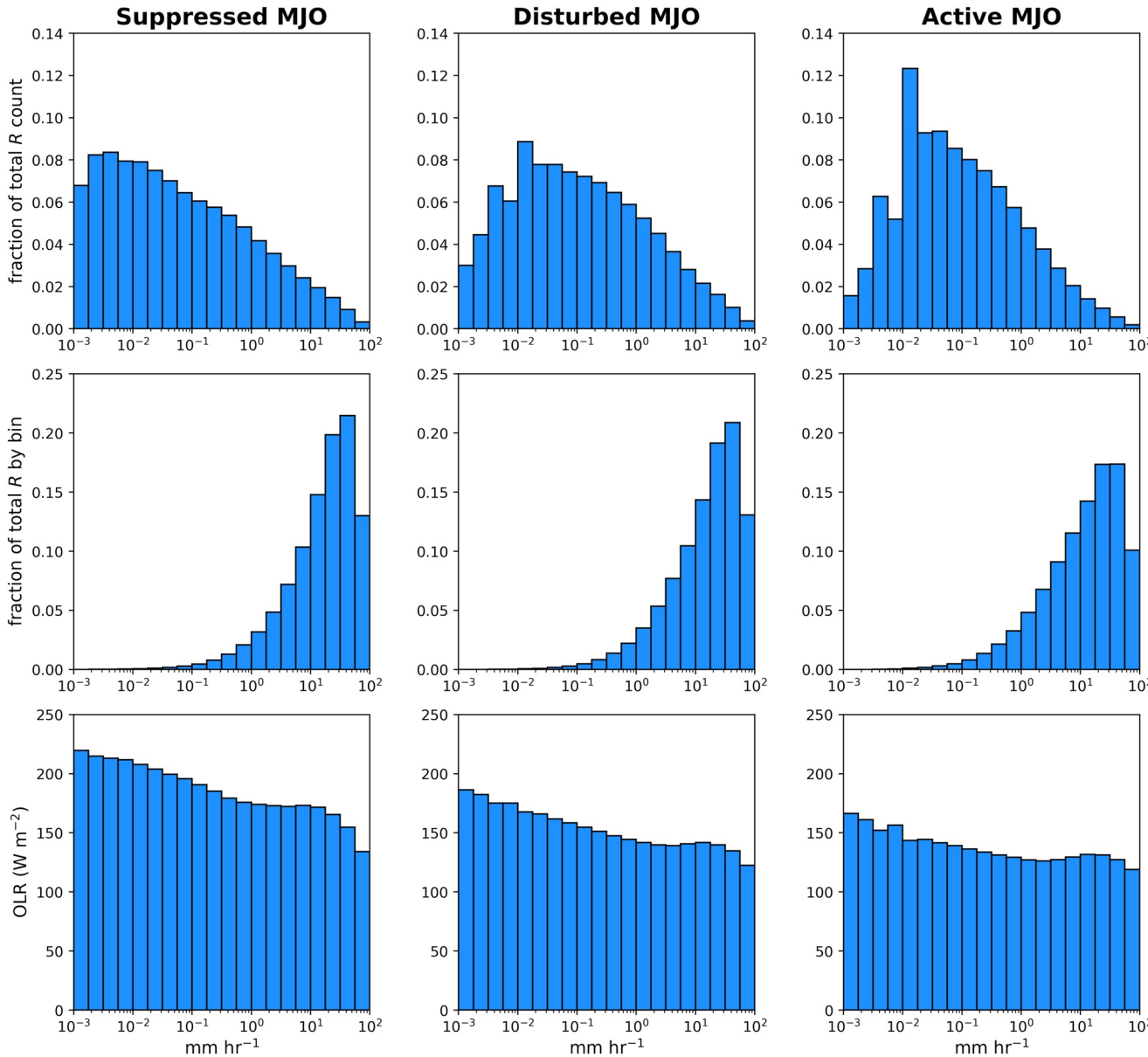

Figure 9. From top row to bottom row: rain rate frequency, contribution to rainfall total by bin, and outgoing longwave radiation, all binned by rain rate and composited column-wise by Madden-Julian Oscillation phase.

strongly stratified by salinity, they inhibit deep vertical mixing by nocturnal convection (Thompson et al., 2019). This allows for the accumulation of subsurface ocean heat in *RL* relative to *no-RL* during the MJO suppressed and disturbed phases. With the arrival of the MJO active phase, the upper ocean is generally well-mixed by wind in both *RL* and *no-RL*, with some transient stabilization present during the lull between the two Kelvin waves (Figure 8).

3.2.3. RL Feedbacks to MJO Convection

To this point, it remains unclear if RL-induced changes to SST and OHC influence the structure and organization of convection. Qualitative comparisons of domain mean rain rate time series between *RL* and *no-RL* are inconclusive (Figure 5) and total accumulated rainfall in the two simulations is similar (∼1% less total rainfall in *RL*). To expand our investigation of RL feedbacks to convection over the MJO lifecycle, we evaluate select atmospheric variables as a function of both MJO phase and rain rate. Figure 9 shows, for the *RL* simulation and each MJO phase, from top row to bottom row: rain rate frequency, fractional contribution to total rainfall by rain rate, and mean OLR as a function of rain rate. Very light rain rates ($R < 0.01$ mm hr^{-1}) dominate the rain rate frequency

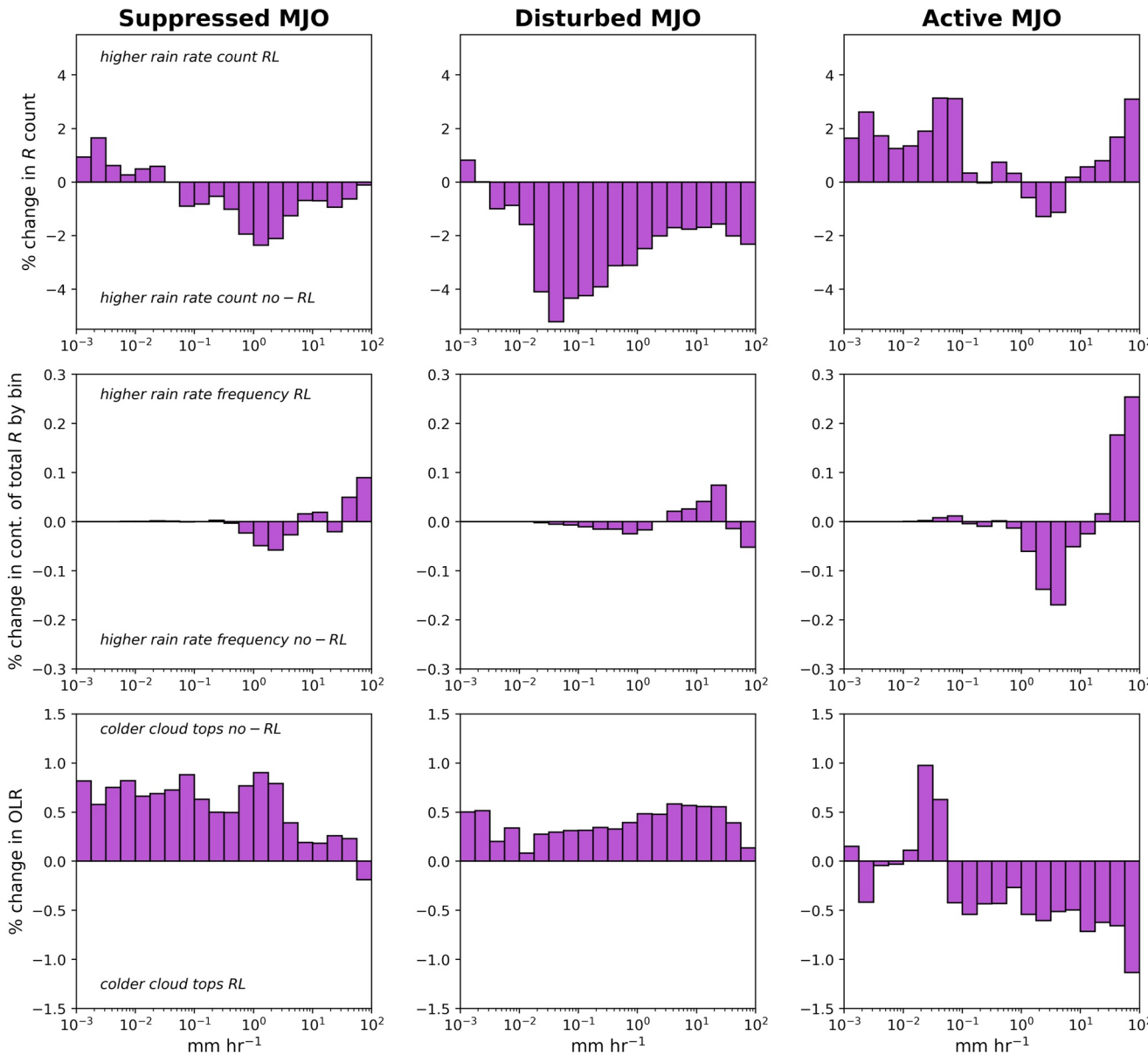

Figure 10. Same as for Figure 9, but as percent change between rain layer (*RL*) and *no-RL*.

distribution during the MJO suppressed phase, but the distribution peak shifts toward higher rain rates (0.01 mm $hr^{-1} < R < 1$ mm hr^{-1}) during the MJO disturbed and active phases. Fractional contribution to total rainfall by rain rate (Figure 9, middle row) varies little with MJO phase, although intermediate rain rates (1–10 mm hr^{-1}) make a relatively larger contribution to total rainfall during the MJO active phase, while heavy rain rates (> 10 mm hr^{-1}) make a relatively smaller contribution. Mean OLR binned by rain rate decreases as rain rate increases for all MJO phases, with the lowest mean OLR values occurring during the MJO active phase.

We compute changes in rain rate frequency, fractional contribution to total rainfall by rain rate, and mean OLR by rain rate between *RL* and *no-RL* to asses the role of the SST effect in regulating convection across MJO phase. Figure 10 shows the same distributions as Figure 9, but as percent change per rain rate bin between *RL* and *no-RL*. For the same rain rate bins, cloud top temperatures in *RL* are higher than those in *no-RL* during the MJO suppressed and disturbed phases, while cloud top temperatures are lower in *RL* during the MJO active phase. This suggests that for the same rain rate, clouds in *RL* are shallower than *no-RL* during MJO suppressed and disturbed phases, and deeper during the MJO active phase. Figure 10 also shows that there is less rainfall in *RL* during the suppressed and disturbed phases and more rainfall in *RL* during the active phase. Furthermore, the underlying

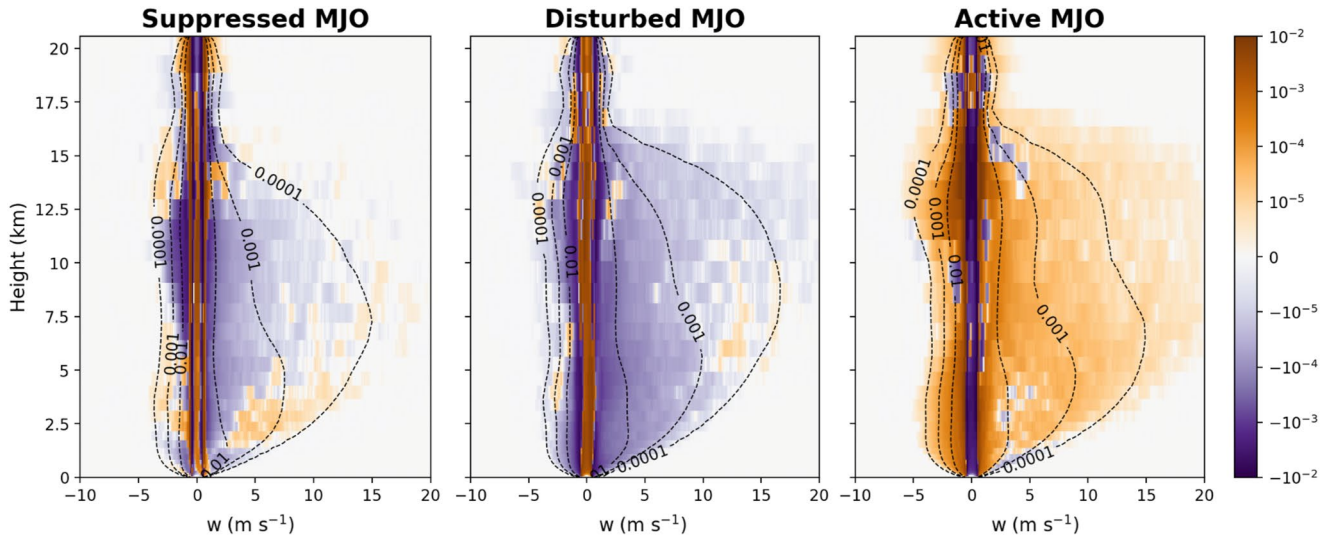

Figure 11. Dashed lines display a contoured frequency by altitude diagram of vertical velocity frequency at different heights in the rain layer (*RL*) simulation. Vertical velocity is binned at 0.1 m s^{-1} intervals and normalized by the total count at each height level in each Madden-Julian Oscillation phase. Bins are then smoothed using a running mean over 1 m s^{-1} intervals at each height. Colored contours display the percent change in vertical velocity frequency (*RL*−*no-RL*). Orange regions represent a higher bin frequency in *RL*, while purple regions represent a higher bin frequency in *no-RL*. Note that the colorbar uses a symmetrical log scale, where values between $\pm 10^{-7}$ are linearly spaced.

contribution of rain rate bins to total rainfall is shifted toward heavier rain rates in *no-RL* during the disturbed phase and heavier rain rates in *RL* during the active phase (Figure 10). These differences are consistent with the SST effect, wherein lower SSTs in RLs during the disturbed phase reduce the frequency and depth of precipitating clouds, and higher SSTs during the active phase increase the frequency and depth of precipitating clouds.

While the rainfall rate perspective offered in Figure 10 suggests RLs do modify convection during the MJO lifecycle through the SST effect, it is also important to analyze changes to vertical structure of convection. We evaluate RL influence on the vertical structure of convection by viewing changes in the vertical velocity (w) distribution between *RL* and *no-RL* as a function of MJO phase. Figure 11 displays a contoured frequency by altitude diagram (Yuter & Houze, 1995) of w frequency by height (dashed lines), and change in w frequency (*RL*−*no-RL*) binned by w and height. During the MJO suppressed phase, bin frequency at w values >2 m s^{-1} are higher in *RL* at low-levels (<5 km), but bin frequency at extreme values are generally reduced at upper levels in *RL* relative to *no-RL* (Figure 11). The broader distribution of w at low-levels in *RL* may be indicative of the SST gradient effect enhancing low-level convergence under weak atmospheric forcing (Figure 3). When the MJO is in the disturbed phase, the frequency of w values >2 m s^{-1} is reduced by an average of 3.45% between ∼5 km and ∼13 km in RL relative to no-RL, supporting the idea that RL-driven SST reduction inhibits deep convection and narrows the w distribution. When the MJO is in the active phase, the frequency of w values >2 m s^{-1} is increased by an average of 2.46% between ∼5 km and ∼13 km in *RL*, as RL modification of ocean temperature and SST broadens the w distribution and enhances deep convection during the MJO active phase.

4. Discussion

We performed regional ocean-atmosphere coupled simulations of the MJO event observed over the tropical Indian Ocean during the November 2011 DYNAMO field campaign to understand how rain falling onto the ocean surface affects atmospheric convection throughout the MJO lifecycle. In the first experiment, rain was allowed to fall onto the ocean surface, forming rain layers (the "*RL*" simulation). In the second experiment, ocean surface freshening by rainfall was turned off, inhibiting the formation of rain layers (the "*no-RL*" simulation).

Previous work has shown that RLs are cooler than the surrounding sea surface (Pei et al., 2018; Shackelford et al., 2022). SST cooling in RLs occurs through RLs salinity stratification that confines evaporative cooling to the 1–2 m deep RL by restricting the downward mixing of near-surface water. We hypothesized that RLs could feed back to MJO convection through two competing mechanisms: first, via the SST gradient effect, wherein SST

gradients generated by RL cool patches enhance boundary layer convergence over the RL-adjacent higher SST regions and facilitate the initiation of convection; and second, via the SST effect, wherein SST reductions within RLs reduced the buoyancy of plumes rising from the boundary layer, thereby limiting the vertical development of convection.

RLs and their associated SST gradients begin to form during the MJO suppressed phase, but are most prevalent during the MJO ocean disturbed phase, which corresponds to the atmospheric convection suppressed-to-deep transition phase. If the SST gradient mechanism is important for atmospheric convection, it would be reflected in more frequent and more vigorous convection in the RL simulation, as measured by an increase in cold cloud fraction (*CCF*) and a broadening of the distribution of vertical velocity (w) throughout the troposphere. Instead, RLs are associated with a decrease in *CCF* during MJO suppressed and disturbed phases (Table 2), and a narrowing of the w distribution for all heights during the MJO disturbed phase (Figure 11). The strongest evidence for the SST gradient effect is seen during the MJO suppressed phase in the broader w distribution with RLs below 5 km (Figure 11). We conclude that, while the SST gradient effect appears to invigorate shallow convection during the MJO suppressed phase when free tropospheric forcing is weak, it does not appear to enhance convection during the MJO disturbed/transition phase when free tropospheric forcing is enhanced.

The RL-affected direct SST effect, wherein cool RLs reduce SST and the vigor of atmospheric convection, appears to be the more important RL feedback pathway for convection, but this mechanism proved to involve unanticipated nuances of how the ocean regulates atmospheric convection. The lower SST (Figures 5 and 6; Table 2), reduced *CCF* (Table 2), and narrower w distribution (Figure 11) in *RL* during the MJO disturbed phase are all consistent with the direct SST effect. As previously noted in Shackelford et al., 2022, the stably stratified upper ocean in RLs reduces vertical mixing below the RL, subsequently leading to a warmer subsurface ocean in *RL* than in *no-RL* during the MJO disturbed phase (Figure 6). However, the disturbed phase also features a 22% increase in net surface heating in *RL* compared to *no-RL* (Table 2). Roughly half of this increase comes from increased net surface shortwave radiation into the ocean in *RL* (Table 2). We attribute the increase in net surface shortwave heating in *RL* to the reduction in *CCF* that allows more incoming solar radiation to reach the ocean surface. RL shoaling of the ocean mixed-layer depth allows the increased surface shortwave radiation to penetrate below the RL base and heat the subsurface ocean, while RL interruption of the diurnal cycle of nocturnal convection insulates subsurface heat from surface evaporative cooling (Figure 8). In essence, RLs cool the ocean surface while simultaneously warming the subsurface ocean (Figure 12). RLs thus act as a "cool lid" on the ocean surface that prevents the atmosphere from accessing subsurface ocean heat.

The direct weakening of convection by RLs and the associated subsurface ocean warming sets up the delayed SST effect. This mechanism is activated by the onset of westerly wind bursts that erode RLs and expose subsurface ocean heat content to the atmosphere that was previously shielded by disturbed phase RLs. The transfer of greater ocean heat content in *RL* to the atmosphere is reflected in greater CCF (Table 2) and a broader w distribution (Figure 11) in *RL* compared to *no-RL* during the MJO active phase. Through this feedback mechanism, RLs lead to more vigorous convection during the MJO active phase.

Our findings are relevant for understanding processes that regulate MJO periodicity and intensity. It is clear that RLs in our experiments delay the onset of deep convection, but then help maintain its intensity once developed. The delay in the onset of deep convection could slow the development of the east-of-convection atmospheric Kelvin wave response to heating and its associated low-level convergence that regulates MJO eastward propagation (Chen & Wang, 2020; Wang & Rui, 1990b; Wang & Xie, 1998), thus reducing MJO propagation speed compared to that of convectively coupled Kelvin waves (Roundy, 2020; Roundy & Frank, 2004; Wheeler & Kiladis, 1999).

Results of our study may also be relevant for understanding some common biases in MJO simulation with global coupled models. Most models tend to overestimate MJO eastward propagation speed and underestimate MJO intensity (Ahn et al., 2017; Ahn et al., 2020; Wang et al., 2018). Vertical resolution of the upper ocean in these models is typically 0(10 m) (Danabasoglu et al., 2020; Klingaman et al., 2011), which is not sufficient to capture the vertical salinity gradients formed by RLs. Hence, rainfall in these models is not likely to stratify the upper ocean, thus inhibiting the RL-induced surface cooling during the MJO disturbed/transition phase. These models, therefore, will not capture the RL-reduced SST during the MJO disturbed/transition phase, nor the subsequent reduction in *CCF*, increase in ocean surface shortwave heating, reduction in subsurface ocean vertical mixing,

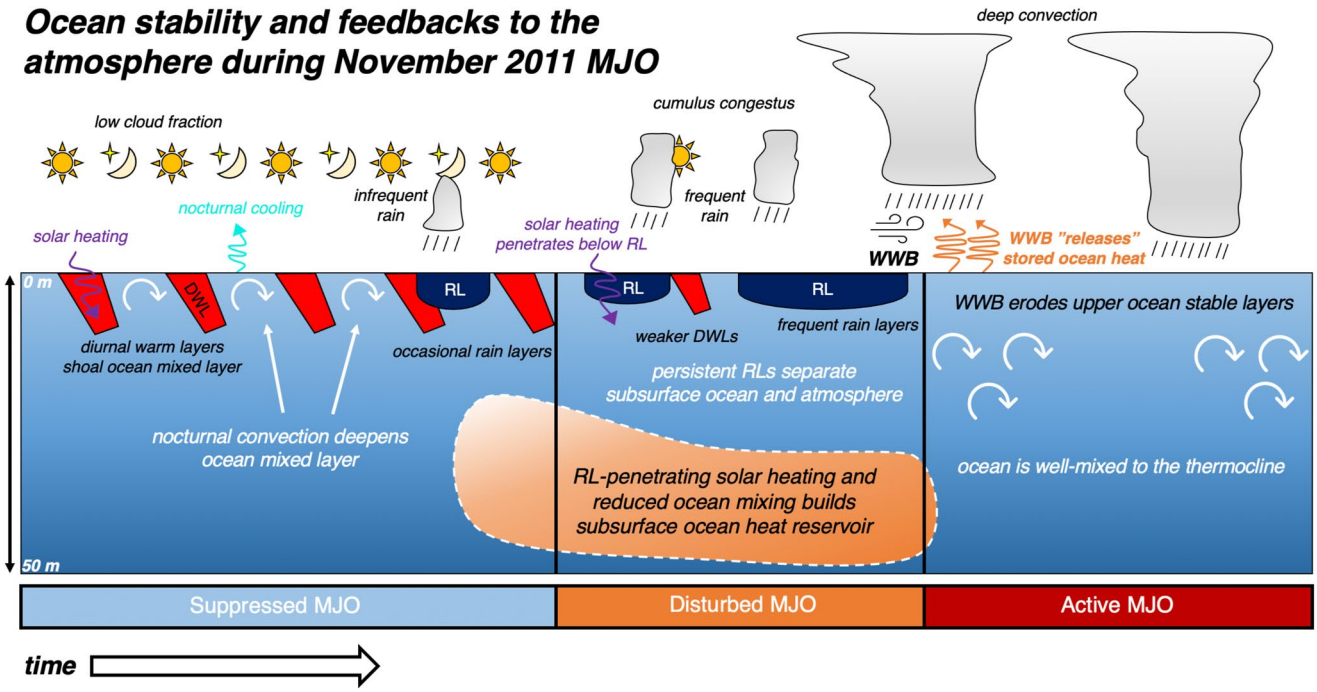

Figure 12. Schematic illustration of the time evolution of ocean stability and rain layer feedbacks to the Madden-Julian Oscillation (MJO) during the November 2011 MJO event from a Eulerian viewpoint. MJO phase is denoted by the colorbar and time moves from left to right. While the November 2011 MJO event is shown here, the physical mechanisms also broadly apply to the MJO in general.

and enhancement of subsurface ocean heat. The lack of these RL-induced processes is consistent with a reduced MJO periodicity (i.e., more rapid eastward propagation) and reduced MJO intensity.

Improved MJO representation in coupled simulations with high resolution vertical grid-spacing in the upper ocean is typically attributed to better resolving the diurnal cycle in SST (Klingaman et al., 2011; Woolnough et al., 2007). We speculate that, in addition to resolving SST diurnal cycle and DWLs, resolving RL-induced SST changes may also be responsible for improved MJO simulation in these cases. Recent efforts to parameterize the effects of RLs on SST (Bellenger et al., 2016; Witte et al., 2023) may mitigate the need for fine ocean vertical resolution, and thus improve MJO simulation when these parameterizations are incorporated into coupled models. We speculate that refinements to ocean vertical resolution or adoption of RL parameterizations in coupled forecast models could also lead to improved forecasts of MJO teleconnections, as part of the challenge of these forecasts lies in correctly simulating the MJO itself (e.g., Wang et al., 2020).

RLs may also interact with other forms of convective organization. Previous studies have noted that ocean coupling may delay or inhibit convective aggregation (Coppin & Bony, 2018; Holloway et al., 2017; Wing et al., 2017), and some studies attribute this delay to SST gradients inducing low-level circulation patterns that oppose patterns favoring convective aggregation (Hogenegger & Stevens, 2016). Additionally, RL enhancement of SSTs during the MJO active phase is qualitatively consistent with similar experiments investigating the influence of salinity stratification on tropical cyclone (TC) intensity. For example, Balaguru et al. (2022) found that salinity stratification in a *RL*-type simulation led to weaker SST reductions beneath the TC compared to a *no-RL*-type simulation, and thus promoted TC intensification. Future work could focus on RL influence on convective organization, as well as the generality of RL formation and feedbacks in regions of more complex ocean dynamics and air-sea interactions, such as the Maritime Continent.

5. Conclusions and Summary

We used a regional coupled atmosphere-ocean model to demonstrate that ocean surface RLs influence the evolution of atmospheric convection over the Indian Ocean associated with the MJO. We conducted two model simulations to evaluate RL feedbacks to the atmosphere and MJO convection: one in which rainfall freshens and cools the ocean surface (*RL*), and a second in which rain freshening and cooling of the ocean surface is disabled

(*no-RL*). These experiments revealed two pathways in which RLs influence atmospheric convection, termed the SST gradient effect and the SST effect.

The SST gradient effect refers to the hydrostatic adjustment of the atmospheric boundary layer to small-scale, rain-induced SST gradients, which has the potential to induce patterns of low-level convergence that excite atmospheric convection. Rain-induced SST gradients are most prominent during the MJO disturbed phase, as evidenced by a factor of four increase in the $\nabla^2 SST$ width parameter in *RL* compared to *no-RL*. However, the disturbed phase features reduced 10 m divergence variance and a narrower distribution of vertical velocity (w) throughout the atmospheric column in *RL* compared to *no-RL*. The SST gradient effect is only detected during the MJO suppressed phase, when enhanced SST gradients with RLs coincide with increased low-level divergence variance and a broadened distribution of w below 5 km.

The SST effect refers to both the direct influence of RL-driven SST reductions on atmospheric convection, and the delayed influence that RL-induced upper ocean stabilization exerts on SST. The direct SST effect is readily apparent during the MJO disturbed phase, when RLs are frequently present and reduce domain mean SST by 0.03 K in *RL* compared to *no-RL*, leading to reduced cold cloud fraction (−3%) and a narrowing of the w distribution throughout the column. Concurrent with reduced SST in *RL* during the disturbed phase is a 0.15%–0.20% increase in upper ocean heat content (0–40 m) in *RL* relative to *no-RL*. Accumulated subsurface ocean heat in *RL* is isolated from the atmosphere by statically stable RLs until the arrival of westerly wind bursts at the onset of the MJO active phase erodes RLs and releases subsurface heat to the ocean surface, raising domain average SST by 0.02 K in *RL* compared to *no-RL* during the active phase. Higher SST in *RL* leads to increased *CCF* (+3%) and broader w distribution throughout the column relative to *no-RL*, thus presenting a delayed pathway in which RLs support the development of deep convection during the MJO active phase.

Data Availability Statement

Model data was obtained by running the Scripps-KAUST Regionally Integrated Prediction System (SKRIPS) coupled model (Sun et al., 2019). SKRIPS code documentation is available here: https://skrips.readthedocs.io/en/v1.2/.

Acknowledgments
We acknowledge and thank Mark Branson and the NCAR CISL helpdesk for their support in porting SKRIPS to NCAR's Cheyenne HPC environment. We would also like to acknowledge and thank Eric Maloney for insightful comments and feedback on this work. This work is supported by NSF Physical Oceanography division (Grant 1924659).

References

Ahn, M.-S., Kim, D., Kang, D., Lee, J., Sperber, K. R., Gleckler, P. J., et al. (2020). MJO propagation across the maritime continent: Are CMIP6 models better than CMIP5 models? *Geophysical Research Letters*, *47*(11), e2020GL087250. https://doi.org/10.1029/2020GL087250

Ahn, M.-S., Kim, D., Sperber, K. R., Kang, I.-S., Maloney, E., Waliser, D., & Hendon, H. (2017). MJO simulation in CMIP5 climate models: MJO skill metrics and process-oriented diagnosis. *Climate Dynamics*, *49*(11–12), 4023–4045. https://doi.org/10.1007/s00382-017-3558-4

Anderson, S. P., Weller, R. A., & Lukas, R. B. (1996). Surface buoyancy forcing and the mixed layer of the western Pacific warm pool: Observations and 1d model results. *Journal of Climate*, *9*(12), 3056–3085. https://doi.org/10.1175/1520-0442(1996)009<3056:sbfatm>2.0.co;2

Asher, W. E., Jessup, A., Branch, R., & Clark, D. (2014). Observations of rain-induced near-surface salinity anomalies. *Journal of Geophysical Research: Oceans*, *119*(8), 5483–5500. https://doi.org/10.1002/2014JC009954

Back, L., & Bretherton, C. (2009). On the relationship between SST gradients, boundary layer winds, and convergence over the tropical oceans. *Journal of Climate*, *22*(15), 4182–4196. https://doi.org/10.1175/2009JCLI2392.1

Balaguru, K., Foltz, G. R., Leung, L. R., & Hagos, S. M. (2022). Impact of rainfall on tropical cyclone-induced sea surface cooling. *Geophysical Research Letters*, *49*(10), e2022GL098187. https://doi.org/10.1029/2022GL098187

Bellenger, H., Drushka, K., Asher, W., Reverdin, G., Katsumata, M., & Watanabe, M. (2016). Extension of the prognostic model of sea surface temperature to rain-induced cool and fresh lenses. *Journal of Geophysical Research: Oceans*, *122*(1), 484–507. https://doi.org/10.1002/2016JC012429

Bellenger, H., & Duvel, J. (2009). An analysis of tropical ocean diurnal warm layers. *Journal of Climate*, *22*(13), 3629–3646. https://doi.org/10.1175/2008JCLI2598.1

Bellenger, H., Takayabu, Y., Ushiyama, T., & Yoneyama, K. (2010). Role of diurnal warm layers in the diurnal cycle of convection of the tropical Indian Ocean during MISMO. *Monthly Weather Review*, *138*(6), 2426–2433. https://doi.org/10.1175/2010MWR3249.1

Bernie, D. J., Woolnough, S. J., Slingo, J. M., & Guilyardi, E. (2005). Modeling diurnal and intraseasonal variability of the ocean mixed layer. *Journal of Climate*, *18*(8), 1190–1202. https://doi.org/10.1175/jcli3319.1

Chassignet, E. P., Burlburt, H. E., Smedstad, O. M., Halliwell, G. R., Hogan, P. J., Wallcraft, A. J., et al. (2007). The HYCOM (hybrid coordinate ocean model) data assimilative system. *Journal of Marine Systems*, *65*(1–4), 60–83. https://doi.org/10.1016/j.jmarsys.2005.09.016

Chen, G., & Wang, B. (2020). Circulation factors determining the propagation speed of the Madden–Julian Oscillation. *Journal of Climate*, *33*(8), 3367–3380. https://doi.org/10.1175/JCLI-D-19-0661.1

Coppin, D., & Bony, S. (2018). On the interplay between convective aggregation, surface temperature gradients, and climate sensitivity. *Journal of Advances in Modeling Earth Systems*, *10*(12), 3123–3138. https://doi.org/10.1029/2018ms001406

Cronin, M. F., & McPhaden, M. J. (2002). Barrier layer formation during westerly wind bursts. *Journal of Geophysical Research*, *107*(C12). https://doi.org/10.1029/2001JC001171

Danabasoglu, G., Lamarque, J.-F., Bacmeister, J., Bailey, D. A., Du Vivier, A. K., Edwards, J., et al. (2020). The community earth system model version 2 (CESM2). *Journal of Advances in Modeling Earth Systems*, *12*(2), e2019MS001916. https://doi.org/10.1029/2019MS001916

DeMott, C. A., Benedict, J., Klingaman, N. P., Woolnough, S. J., & Randall, D. A. (2016). Diagnosing ocean feedbacks to the MJO: SST-modulated surface fluxes and the moist static energy budget. *Journal of Geophysical Research: Atmospheres*, *121*(14), 8350–8373. https://doi.org/10.1002/2016JD025098

DeMott, C. A., Klingaman, N. P., Tseng, W.-L., Burt, M. A., Gao, Y., & Randall, D. A. (2019). The convection connection: How ocean feedbacks affect tropical mean moisture and MJO propagation. *Journal of Geophysical Research: Atmospheres*, *124*(22), 11910–11931. https://doi.org/10.1029/2019JD031015

DeMott, C. A., Klingaman, N. P., & Woolnough, S. J. (2015). Atmosphere-ocean coupled processes in the Madden-Julian Oscillation. *Reviews of Geophysics*, *53*(4), 1099–1154. https://doi.org/10.1002/2014RG000478

de Szoeke, S. P., Edson, J. B., Marion, J. R., Fairall, C. W., & Bariteau, L. (2015). The MJO and air–sea interaction in TOGAE COARE and DYNAMO. *Journal of Climate*, *28*(2), 597–622. https://doi.org/10.1175/JCLI-D-14-00477.1

de Szoeke, S. P., & Maloney, E. (2020). Atmospheric mixed layer convergence from observed MJO sea surface temperature anomalies. *Journal of Climate*, *33*(2), 547–558. https://doi.org/10.1175/JCLI-D-19-0351.1

de Szoeke, S. P., Marke, T., & Brewer, W. A. (2021). Diurnal ocean surface warming drives convective turbulence and clouds in the atmosphere. *Geophysical Research Letters*, *48*(4). https://doi.org/10.1029/2020GL091299

Drushka, K., Asher, W., Jessup, A., Thompson, E., Iyer, S., & Clark, D. (2019). Capturing fresh layers with the surface salinity profiler. *Oceanography*, *32*(2), 76–85. https://doi.org/10.5670/oceanog.2019.215

Drushka, K., Asher, W. E., Ward, B., & Walesby, K. (2016). Understanding the formation and evolution of rain-formed fresh lenses at the ocean surface. *Journal of Geophysical Research: Oceans*, *121*(4), 2673–2689. https://doi.org/10.1002/2015JC011527

Fairall, C., Bradley, E., Hare, J., Grachev, A., & Edson, J. (2003). Bulk parameterization of air-sea fluxes for tropical ocean-global atmosphere coupled-ocean atmosphere response experiment. *Journal of Climate*, *16*(4), 571–591. https://doi.org/10.1175/1520-0442(2003)016<0571:BPOASF>2.0.CO;2

Fairall, C., Bradley, E., Rogers, D., Edson, J., & Young, G. (1996). Bulk parameterization of air-sea fluxes for tropical ocean-global atmosphere coupled-ocean atmosphere response experiment. *Journal of Geophysical Research*, *101*(C2), 3747–3764. https://doi.org/10.1029/95JC03205

Gosnell, R., Fairall, C., & Webster, P. (1995). The sensible heat of rainfall in the tropical ocean. *Journal of Geophysical Research: Atmosphere*, *100*(C9), 18437–18442. https://doi.org/10.1029/95JC01833

Halkides, D. J., Waliser, D. E., Lee, T., Menemenlis, D., & Guan, B. (2015). Quantifying the processes controlling intraseasonal mixed-layer temperature variability in the tropical Indian Ocean. *Journal of Geophysical Research: Oceans*, *120*(2), 692–715. https://doi.org/10.1002/2014JC010139

Hersbach, H., Bell, B., Berrisford, P., Hirahara, S., Horányi, A., Muñoz-Sabater, J., et al. (2020). The ERA5 global reanalysis. *Quarterly Journal of the Royal Meteorological Society*, *146*(730), 1999–2049. https://doi.org/10.1002/qj.3803

Hill, C., De Luca, C., BalajiSuarez, M., & Da Silva, A. (2004). The architecture of the earth system modeling framework. *Computing in Science and Engineering*, *6*(1), 18–28. https://doi.org/10.1109/MCISE.2004.1255817

Hogenegger, C., & Stevens, B. (2016). Coupled radiative convective equilibrium simulations with explicit and parameterized convection. *Journal of Advances in Modelling Earth Systems*, *8*(3), 1468–1482.

Holloway, C. E., Wing, A. A., Bony, S., Muller, C., Masunaga, H., L'Ecuyer, T. S., et al. (2017). Observing convective aggregation. *Surveys in Geophysics*, *38*(6), 1199–1236. https://doi.org/10.1007/s10712-017-9419-1

Hoskins, B. J., & Karoly, D. J. (1981). The steady linear response of a spherical atmosphere to thermal and orographic forcing. *Journal of the Atmospheric Sciences*, *38*(6), 1179–1196. https://doi.org/10.1175/1520-0469(1981)038⟨1179:TSLROA⟩2.0.CO;2

Hudson, J., & Maloney, E. (2022). The role of surface fluxes in MJO propagation through the maritime continent. *Journal of Climate*, *36*(6), 1633–1652. https://doi.org/10.1175/JCLI-D-22-0484.1

Iacono, M. J., Delamere, J. S., Mlawer, E. J., Shephard, M. W., Clough, S. A., & Collins, W. D. (2008). Radiative forcing by long-lived greenhouse gases: Calculations with the AER radiative transfer models. *Journal of Geophysical Research*, *113*(D13). https://doi.org/10.1029/2008JD009944

Iyer, S., & Drushka, K. (2021). Turbulence within rain-formed fresh lenses during the SPURS-2 experiment. *Journal of Physical Oceanography*, *51*(5), 1705–1721. https://doi.org/10.1175/JPO-D-20-0303.1

Jiménez, P. A., Dudhia, J., González-Rouco, J. F., Navarro, J., Montávez, J. P., & García-Bustamante, E. (2012). A revised scheme for the WRF surface layer formulation. *Monthly Weather Review*, *140*(3), 898–918. https://doi.org/10.1175/MWR-D-11-00056.1

Johnson, R. H., Rickenbach, T. M., Rutledge, S. A., Ciesielski, P. E., & Schubert, W. H. (1999). Trimodal characteristics of tropical convection. *Journal of Climate*, *12*(8), 2397–2418. https://doi.org/10.1175/1520-0442(1999)012⟨2397:TCOTC⟩2.0.CO;2

Kemball-Cook, S., Wang, B., & Fu, X. (2002). Simulation of the ISO in the ECHAM4 model: The impact of coupling with an ocean model. *Journal of Atmospheric Science*, *59*(9), 1433–1453. https://doi.org/10.1175/1520-0469(2002)059⟨1433:SOTIOI⟩2.0.CO;2

Klingaman, N. P., Woolnough, S. J., Weller, H., & Slingo, J. M. (2011). The impact of finer-resolution air–sea coupling on the intraseasonal oscillation of the Indian monsoon. *Journal of Climate*, *24*(10), 2451–2468. https://doi.org/10.1175/2010JCLI3868.1

Large, W. G., McWilliams, J. C., & Doney, S. C. (1994). Oceanic vertical mixing: A review and a model with a nonlocal boundary layer parameterization. *Reviews of Geophysics*, *32*(4), 363–403. https://doi.org/10.1029/94RG01872

Lau, K. M., & Sui, C. H. (1997). Mechanisms of short-term sea surface temperature regulation: Observations during TOGA COARE. *Journal of Climate*, *10*(3), 465–472. https://doi.org/10.1175/1520-0442(1997)010⟨0465:MOSTSS⟩2.0.CO;2

Li, Y., & Carbone, R. (2012). Excitation of rainfall over the tropical western Pacific. *Journal of the Atmospheric Sciences*, *69*(10), 2983–2994. https://doi.org/10.1175/JAS-D-11-0245.1

Lindzen, R. S., & Nigam, S. (1987). On the role of sea surface temperature gradients in forcing low-level winds and convergence in the tropics. *Journal of the Atmospheric Sciences*, *44*(17), 2418–2436. https://doi.org/10.1175/1520-0469(1987)044⟨2418:OTROSS⟩2.0.CO;2

Lucas-Picher, P., Argüeso, D., Brisson, E., Tramblay, Y., Berg, P., Lemonsu, A., et al. (2021). Convection-permitting modeling with regional climate models: Latest developments and next steps. *WIREs Climate Change*, *12*(6), e731. https://doi.org/10.1002/wcc.731

Madden, R. A., & Julian, P. R. (1971). Detection of a 40–50 day oscillation in the zonal wind in the tropical Pacific. *Journal of the Atmospheric Sciences*, *28*(5), 702–708. https://doi.org/10.1175/1520-0469(1971)028⟨0702:DOADOI⟩2.0.CO;2

Marshall, J., Adcroft, A., Hill, C., Perelman, L., & Heisey, C. (1997). A finite-volume, incompressible Navier Stokes model for studies of the ocean on parallel computers. *Journal of Geophysical Research*, *102*(C3), 5753–5766. https://doi.org/10.1029/96JC02775

McPhaden, M. J., Freitag, H. P., Hayes, S. P., Taft, B. A., Chen, Z., & Wyrtki, K. (1988). The response of the equatorial Pacific Ocean to a westerly wind burst in May 1986. *Journal of Geophysical Research*, *93*(C9), 10589–10603. https://doi.org/10.1029/JC093iC09p10589

Morrison, H., Curry, J. A., & Khvorostyanov, V. I. (2005). A new double-moment microphysics parameterization for application in cloud and climate models. Part I: Description. *Journal of the Atmospheric Sciences*, *62*(6), 1665–1677. https://doi.org/10.1175/JAS3446.1

Moum, J. N., de Szoeke, S. P., Smyth, W. D., Edson, J. B., De Witt, H. L., Moulin, A. J., et al. (2014). Air–sea interactions from westerly wind bursts during the November 2011 MJO in the Indian Ocean. *Bulletin of the American Meteorological Society*, *95*(8), 1185–1199. https://doi.org/10.1175/BAMS-D-12-00225.1

Moum, J. N., Pujiana, K., Lien, R.-C., & Smyth, W. D. (2016). Ocean feedback to pulses of the Madden–Julian oscillation in the equatorial Indian Ocean. *Nature Communications*, *7*(13203), 1185–1199. https://doi.org/10.1038/ncomms13203

Nakanishi, M., & Niino, H. (2009). Development of an improved turbulence closure model for the atmospheric boundary layer. *Journal of the Meteorological Society of Japan*, *87*(5), 895–912. https://doi.org/10.2151/jmsj.87.895

Paulson, C., & Simpson, J. (1977). Irradiance measurements in upper ocean. *Journal of Physical Oceanography*, *7*(6), 952–956. https://doi.org/10.1175/1520-0485(1977)007<0952:imituo>2.0.co;2

Pei, S., Shinoda, T., Soloviev, A., & Lein, R.-C. (2018). Upper ocean response to the atmospheric cold pools associated with the Madden-Julian Oscillation. *Geophysical Research Letters*, *45*(10), 5020–5029. https://doi.org/10.1029/2018GL077825

Pujiana, K., Moum, J. N., & Smyth, W. D. (2018). The role of turbulence in redistributing upper-ocean heat, freshwater, and momentum in response to the MJO in the equatorial Indian Ocean. *Journal of Physical Oceanography*, *48*(1), 197–220. https://doi.org/10.1175/JPO-D-17-0146.1

Reverdin, G., Morisset, S., Boutin, J., & Martin, N. (2012). Rain-induced variability of near sea-surface t and s from drifter data. *Journal of Geophysical Research*, *117*(C2). https://doi.org/10.1029/2011JC007549

Roundy, P. E. (2020). A climatology of waves in the equatorial region. *Quarterly Journal of the Royal Meteorological Society*, *146*(727), 795–806. https://doi.org/10.1002/qj.3709

Roundy, P. E., & Frank, W. M. (2004). A climatology of waves in the equatorial region. *Journal of the Atmospheric Sciences*, *61*(17), 2105–2132. https://doi.org/10.1175/1520-0469(2004)061⟨2105:ACOWIT⟩2.0.CO;2

Ruppert, J. H., Jr., & Johnson, R. H. (2016). On the cumulus diurnal cycle over the tropical warm pool. *Journal of Advances in Modeling Earth Systems*, *08*(2), 669–690. https://doi.org/10.1002/2015MS000610

Shackelford, K., De Mott, C. A., van Leeuwen, P. J., Thompson, E., & Hagos, S. (2022). Rain-induced stratification of the equatorial Indian Ocean and its potential feedback to the atmosphere. *Journal of Geophysical Research: Oceans*, *127*(3), e2021JC018025. https://doi.org/10.1029/2021JC018025

Skamarock, W. C., Klemp, J. B., Dudhia, J., Gill, D. O., Liu, Z., Berner, J., et al. (2019). A description of the advanced research WRF version 4. Note NCAR/TN-556+STR. *NCAR Tech*, 145. https://doi.org/10.5065/1dfh-6p97

Soloviev, A., & Lukas, R. (1997). Observation of large diurnal warming events in the near-surface layer of the western equatorial Pacific warm pool. *Deep Sea Research Part I: Oceanographic Research Papers*, *44*(6), 1055–1076. https://doi.org/10.1016/S0967-0637(96)00124-0

Sprintall, J., & Tomczak, M. (1992). Evidence of the barrier layer in the surface layer of the tropics. *Journal of Geophysical Research*, *97*(C5), 7305–7316. https://doi.org/10.1029/92JC00407

Stan, C., Zheng, C., Chang, E. K.-M., Domeisen, D. I., Garfinkel, C. I., Jenney, A. M., et al., (2022). Advances in the prediction of MJO teleconnections in the S2S forecast systems. *Bulletin of the American Meteorological Society*, *103*(6), E1426–E1447. https://doi.org/10.1175/bams-d-21-0130.1

Sun, R., Subramanian, A. C., Cornuelle, B. D., Mazloff, M. R., Miller, A. J., Ralph, F. M., et al. (2021). The role of air–sea interactions in atmospheric rivers: Case studies using the SKRIPS regional coupled model. *Journal of Geophysical Research: Atmospheres*, *126*(6), e2020JD032885. https://doi.org/10.1029/2020JD032885

Sun, R., Subramanian, A. C., Miller, A. J., Mazloff, M. R., Hoteit, I., & Cornuelle, B. D. (2019). SKRIPS v1.0: A regional coupled ocean–atmosphere modeling framework (MITGCM–WRF) using ESMF/NUOPC, description and preliminary results for the Red Sea. *Geoscientific Model Development*, *12*(10), 4221–4244. https://doi.org/10.5194/gmd-12-4221-2019

Thompson, E. J., Moum, J. N., Fairall, C. W., & Rutledge, S. A. (2019). Wind limits on rain layers and diurnal warm layers. *Journal of Geophysical Research: Oceans*, *124*(2), 897–924. https://doi.org/10.1029/2018JC014130

Tseng, K.-C., Maloney, E., & Barnes, E. (2019). The consistency of MJO teleconnection patterns: An explanation using linear Rossby wave theory. *Journal of Climate*, *32*(2), 531–548. https://doi.org/10.1175/jcli-d-18-0211.1

Vitart, F. (2017). Madden—Julian oscillation prediction and teleconnections in the S2S database. *Quarterly Journal of the Royal Meteorological Society*, *143*(706), 2210–2220. https://doi.org/10.1002/qj.3079

Wang, B., & Rui, H. (1990). Dynamics of the coupled moist Kelvin–Rossby wave on an equatorial b-plane. *Journal of the Atmospheric Sciences*, *47*(4), 397–413. https://doi.org/10.1175/1520-0469(1990)047<0397:dotcmk>2.0.co;2

Wang, B., & Rui, H. (1990). Synoptic climatology of transient tropical intraseasonal convective anomalies. *Meteorology and Atmospheric Physics*, *44*(1–4), 43–61. https://doi.org/10.1007/BF01026810

Wang, B., & Xie, X. (1998). Coupled modes of the warm pool climate system. Part I: The role of air–sea interaction in maintaining Madden–Julian Oscillation. *Journal of Climate*, *11*, 2116–2135. https://doi.org/10.1175/1520-0442(1998)011⟨2116:CMOTWP⟩2.0.CO;2

Wang, J., Kim, H., Kim, D., Henderson, S. A., Stan, C., & Maloney, E. D. (2020). MJO teleconnections over the PNA region in climate models. Part I: Performance- and process-based skill metrics. *Journal of Climate*, *33*(3), 1051–1067. https://doi.org/10.1175/JCLI-D-19-0253.1

Wang, S., Ma, D., Sobel, A. H., & Tippett, M. K. (2018). Propagation characteristics of BSISO indices. *Geophysical Research Letters*, *45*(18), 9934–9943. https://doi.org/10.1029/2018GL078321

Weickmann, K. M. (1983). Intraseasonal circulation and outgoing longwave radiation modes during northern hemisphere winter. *Monthly Weather Review*, *111*, 1838–1858. https://doi.org/10.1175/1520-0493(1983)111⟨1838:ICAOLR⟩2.0.CO;2

Weller, R., & Anderson, S. (1996). Surface meteorology and air-sea fluxes in the western equatorial Pacific warm pool during the TOGA Coupled Ocean-Atmosphere Response Experiment. *Journal of Climate*, *9*(8), 1959–1990. https://doi.org/10.1175/1520-0442(1996)009<1959:smaasf>2.0.co;2

Wheeler, M., & Kiladis, G. N. (1999). Convectively coupled equatorial waves: Analysis of clouds and temperature in the wavenumber–frequency domain. *Journal of the Atmospheric Sciences*, *56*(3), 374–399. https://doi.org/10.1175/1520-0469(1999)056⟨0374:CCEWAO⟩2.0.CO;2

Wijesekera, H. W., Paulson, C. A., & Huyer, A. (1999). The effect of rainfall on the surface layer during a westerly wind burst in the western equatorial Pacific. *Journal of Physical Oceanography*, *29*(4), 612–632. https://doi.org/10.1175/1520-0485(1999)029⟨0612:TEOROT⟩2.0.CO;2

Wing, A. A., Emanuel, K., Holloway, C. E., & Muller, C. (2017). Convective self-aggregation in numerical simulations: A review. *Surveys in Geophysics*, *38*(6), 1173–1197. https://doi.org/10.1175/BAMS-D-12-00157.1

Witte, C. R., Zappa, C. J., & Edson, J. B. (2023). The response of ocean skin temperature to rain: Observations and implications for parameterization of rain-induced fluxes. *Journal of Geophysical Research: Oceans*, *128*, e2022JC019146. https://doi.org/10.1029/2022JC019146

Woods, J. D., & Barkmann, W. (1986). The response of the upper ocean to solar heating. I: The mixed layer. *Quarterly Journal of Royal Meteorological Society*, *112*(471), 1–27. https://doi.org/10.1002/qj.49711247102

Woolnough, S., Slingo, J., & Hoskins, B. (2000). The relationship between convection and sea surface temperature on intraseasonal timescales. *Journal of Climate*, *13*, 2086–2104. https://doi.org/10.1175/1520-0442(2000)013⟨2086:TRBCAS⟩2.0.CO;2

Woolnough, S., Vitart, F., & Balmaseda, M. A. (2007). The role of the ocean in the Madden-Julian Oscillation: Implications for MJO prediction. *Quarterly Journal of the Royal Meteorological Society*, *133*, 117–128. https://doi.org/10.1175/1520-0485(1999)029⟨0612:TEOROT⟩2.0.CO;2

Yoneyama, K., Zhang, C., & Long, C. (2013). Tracking pulses of the Madden-Julian Oscillation. *Bulletin of the American Meteorological Society*, *94*(12), 1871–1891. https://doi.org/10.1175/BAMS-D-12-00157.1

You, Y. (1998). Rain-formed barrier layer of the western equatorial Pacific warm pool: A case study. *Journal of Geophysical Research*, *103*(C3), 5361–5378. https://doi.org/10.1029/97JC03421

Yuter, S. E., & Houze, R. A., Jr. (1995). Three-dimensional kinematic and microphysical evolution of Florida cumulonimbus. Part II: Frequency distributions of vertical velocity, reflectivity, and differential reflectivity. *Monthly Weather Review*, *123*(7), 1941–1963. https://doi.org/10.1175/1520-0493(1995)123<1941:tdkame>2.0.co;2

Zhang, C., & Anderson, S. P. (2003). Sensitivity of intraseasonal perturbations in SST to the structure of the MJO. *Journal of the Atmospheric Sciences*, *60*(17), 2196–2207. https://doi.org/10.1175/1520-0469(2003)060⟨2196:SOIPIS⟩2.0.CO;2

Zhang, C., Dong, M., Gualdi, S., Hendon, H. H., Maloney, E. D., Marshall, A., et al. (2006). Simulations of the Madden-Julian Oscillation in four pairs of coupled and uncoupled global models. *Climate Dynamics*, *27*(17), 573–592. https://doi.org/10.1007/s00382-006-0148-2

Zhao, N., & Nasuno, T. (2020). How does the air-sea coupling frequency affect convection during the MJO passage? *Journal of Advances in Modeling Earth Systems*, *12*(4). https://doi.org/10.1029/2020MS002058